Thermodynamic Stabilities of Perfect and Vacancy-Defected Li_{2}TiO_{3} (001) Surfaces From First-Principles Analyses

Yan Jiang, Yanli Shi, Xiaogang Xiang, Jianqi Qi, Yong Han, Zhijun Liao, and Tiecheng Lu

Phys. Rev. Applied **11**, 054088 — Published 31 May 2019

DOI: 10.1103/PhysRevApplied.11.054088

Thermodynamic stabilities of perfect and vacancy-defected Li_2TiO_3 (001) surfaces from first-principles analyses

Yan Jiang,[1,2] Yanli Shi,[1,2] Xiaogang Xiang,[3] Jianqi Qi,[1,3] Yong Han,[4,5,*] Zhijun Liao,[1,2] and Tiecheng Lu,[1,2,3]

[1]*College of Physical Science and Technology, Sichuan University, Chengdu 610064, Sichuan, P. R. China*

[2]*Key Laboratory of Radiation Physics and Technology of Ministry of Education, Sichuan University, Chengdu 610064, Sichuan, P. R. China*

[3]*Key Laboratory of High Energy Density Physics of Ministry of Education, Sichuan University, Chengdu 610064, Sichuan, P. R. China*

[4]*Ames Laboratory, U. S. Department of Energy, Iowa State University, Ames, Iowa 50011, United States*

[5]*Department of Physics and Astronomy, Iowa State University, Ames, Iowa 50011, United States*

Lithium titanate (Li_2TiO_3) is an attractive ceramic material for various industrial applications, particularly as one of most promising breeder blanket materials in future nuclear fusion reactors. Previously-reported studies mainly focus on sintered polycrystalline samples of Li_2TiO_3. Surface structure of the single-crystal form is rarely reported, although the information of surface structures and stabilities can be critical for further understanding the surface-associated processes. In this work, we perform extensive first-principles density-functional-theory (DFT) calculations to obtain the surface energies of Li_2TiO_3 (001) with different surface terminations. For four perfect (defect-free) Li-, O-, or LiTi-terminated (001) surfaces, Li- or O-terminated (001) surfaces can be most stable in a limited chemical-potential ranges corresponding to certain experimental conditions, while LiTi-terminated (001) surface is always unfavorable relative to Li or O terminations. By calculating total energies of various possible configurations with surface vacancies, we determine the energetically-most-favorable vacancy-defected surface terminations. From the corresponding ternary phase diagram, we analyze the stability of a specific surface termination with vacancies as well as the possible formation of oxides. Our stability analysis together with DFT-simulated scanning-tunneling-microscope (STM) images reveals that a 1/3-monolayer-Li-terminated surface most likely corresponds to the ordered hexagonal-like pattern observed previously in STM experiments. For a 1/2-monolayer-Li-terminated surface, the most-stable surface structure from our DFT calculations contrasts with previous result from an empirical-potential model.

* y27h@ameslab.gov

I. INTRODUCTION

Lithium titanate (Li_2TiO_3) has numerous practical and potential industrial applications. Among these applications, Li_2TiO_3 has been considered as one of most promising breeder blanket materials in future nuclear fusion reactors due to its great material performance including reasonable lithium density, high melting temperature, low activation, good chemical stability, good structural compatibility, and excellent tritium release performance [1, 2, 3, 4, 5, 6]. Amongst its already-realized applications, Li_2TiO_3 has been used as an electrode material for molten carbonate fuel cells [7, 8] and for fast-recharging Li-ion batteries [9, 10, 11, 12]. Recently, Li_2TiO_3 has also been proposed as a good candidate of microwave dielectric material related to wireless and mobile communication [13], as well as a suitable electrode material for supercapattery application [14].

Most of previously-reported studies have focused on sintered polycrystalline samples of Li_2TiO_3. Such samples do not provide information about the surface structure at the atomic scale, while the specific atomic-scale surface structure is undoubtedly critical for further studying surface-associated processes, such as adsorption, diffusion, desorption, or reaction of hydrogen isotopes, hydroxyl groups, water molecules, or Li atoms on or near the surface [15, 16, 17, 18].

So far, the only reported experimental study for atomic-scale surface structure of Li_2TiO_3 is from Azuma *et al*. [19] They used low-energy electron diffraction (LEED) and scanning tunneling microscopy (STM) to investigate the structure of the monoclinic Li_2TiO_3 (001) surface under ultrahigh vacuum conditions at room temperature. Their LEED experiment showed a well-ordered Li_2TiO_3 (001) surface by annealing at 1200 K, and their STM images showed terraces with step heights from 0.2 to 0.3 nm. From their STM images after annealing to 1400 K, ordered hexagonal-like patterns with a periodicity of about 0.5 nm are observed. They attempted to interpret these observed patterns using the empirical-potential molecular dynamics (MD) simulations. In a separate work [20], Azuma *et al*. performed first-principles density-functional-theory (DFT) calculations for the surface terminations of Li_2TiO_3 (001). However, they only calculate a few terminations of stoichiometric Li_2TiO_3 (001) surfaces, and therefore provide very limited information to describe the stability of a specific surface termination. Also, we did not find any comparison between their DFT results and the above experimental observations or the empirical-potential MD-simulated results. Thus, in this work, we perform a systematic first-principles DFT analysis for various perfect (defect-free) and vacancy-defected terminations of Li_2TiO_3 (001) surfaces and provide insights for the stabilities of surface structures with considerations of the above experimental observations.

In Azuma *et al*.'s experimental work [19], single crystals of monoclinic Li_2TiO_3

with a space group of C2/c were grown. In our present work, therefore, we focus on the monoclinic Li_2TiO_3, which is actually a stable phase throughout the operating temperature range of a breeder material [21, 22]. The single-crystal Li_2TiO_3 unit cell contains eight formula units (consisting of 48 atoms) with the experimental lattice parameters: a = 0.50623 nm, b = 0.87876 nm, c = 0.97533 nm, and β = 100.212° at 295 K [21]. Along the ⟨001⟩ direction, the crystal structure of Li_2TiO_3 features the -(Li-O-LiTi-O)-(Li-O-LiTi-O)- stacking sequence with the three different types of atomic monolayer: Li, LiTi, or O monolayer, as illustrated in Fig. 1. A Li (O) monolayer is occupied exclusively by lithium (oxygen) atoms. In a LiTi monolayer, 1/3 of the lattice sites are occupied by lithium atoms and 2/3 by titanium atoms. Then, the Li_2TiO_3 (001) surface has 4 types of terminations: one type of Li_x termination, two types of O_x terminations, and one type of Li_xTi_y termination, where x or y is the coverage. For a perfect (i.e., defect-free) Li or O termination, x is equal to 1; for a perfect LiTi termination, $x = 1/3$ and $y = 2/3$. For a vacancy-defected Li_x or O_x termination, $0 < x < 1$; for a vacancy-defected Li_xTi_y termination, $0 < x + y < 1$ with $0 \le x \le 1/3$ and $0 \le y \le 2/3$. To identify two distinct O_x terminations, we use the symbols "O_x-LiTi" and "O_x-Li" to denote them, i.e., the first two monolayers at the surface are implied. Along the ⟨001⟩ direction, there are two different interlayer spacings: $d_{Li\text{-}O}$ and $d_{O\text{-}LiTi}$, which are the distances between two nearest neighbor (NN) Li and O monolayers and between two NN O and LiTi monolayers, respectively, as indicated in Fig. 1(b). Using the experimental values of coordinates of atoms [21], one can obtain $d_{Li\text{-}O}$ = 0.1308 nm and $d_{O\text{-}LiTi}$ = 0.1091 nm.

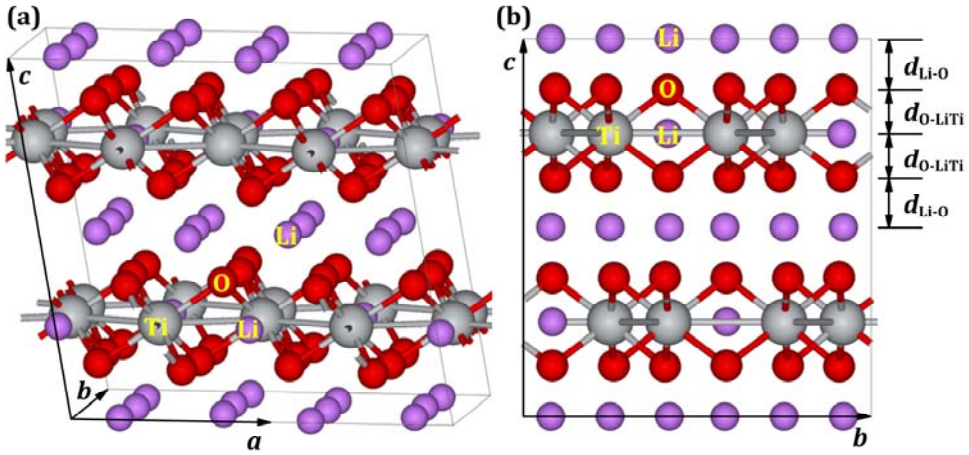

FIG. 1. (a) A 2×1×1 cell of the Li_2TiO_3 single crystal. The types of atoms as well as the translation vectors ***a***, ***b***, and ***c*** of the unit cell (1×1×1) are indicated. The angle between ***a*** and ***c*** is β, while ***a*** and ***b***, or ***b*** and ***c***, are perpendicular to each other. (b) A view along the ⟨001⟩ direction. $d_{Li\text{-}O}$ ($d_{O\text{-}LiTi}$) denotes the interlayer spacings between Li and O (O and LiTi) monolayers.

This paper is organized as follows. Sec. II describes the general thermodynamic formalism for calculating the surface energies of planar surface systems including the Li_2TiO_3 surface system. Sec. III describes the DFT method used in our calculations and makes the benchmark calculations for the bulk properties of various crystals involved in the calculations for Li_2TiO_3 surface energies. Sec. IV presents the results of surface energies for 4 types of perfect terminations of Li_2TiO_3 (001) surface. Sec. V presents the results of surface energies for various vacancy-defected terminations of Li_2TiO_3 (001) surface. Sec. VI is a discussion, involving growth and stabilities of Li_2TiO_3 (001) surface structures which relate previous experimental observations. In Sec. VII, we make a summary.

II. THERMODYNAMIC FORMALISM

From the first and second laws of thermodynamics, for a planar solid-surface system, the Gibbs free energy is given by

$$G = \sum_i N_i \mu_i + \gamma A, \tag{1}$$

where $G \equiv E + PV - TS$ with internal energy E, pressure P, volume V, temperature T, and entropy S; N_i is the number of particles (e.g., atoms) composing the ith chemical component, and μ_i is the chemical potential of the ith chemical component; A is the surface area, and γ is an excess Gibbs free energy per unit area due to the presence of the surface by noting that $\sum_i N_i \mu_i$ is the Gibbs free energy of the same amount of material in a reservoir which is a very large homogeneous dispersed phase (e.g., a gas phase) with the same chemical potential μ_i for any ith chemical component. From Eq. (1), an infinitesimal change in E at constant T and P yields

$$\mathrm{d}E = T\mathrm{d}S - P\mathrm{d}V + \sum_i \mu_i \mathrm{d}N_i + \gamma \mathrm{d}A, \tag{2}$$

which indicates that γ is the change in internal energy E when the area A is reversibly changed for constant entropy S and volume V in a closed system (i.e., constant N_i). Therefore, γ is the work of creating a unit area of a specific surface [23] from a homogeneous dispersed phase when T, P, S, V, and N_i are not changed, and then γ can characterize the "stability" of this surface: lower (higher) γ indicates less (more) work is needed to create the surface and hence the surface is more "stable (unstable)". The quantity γ is usually called the "surface free energy" or "surface energy" of the specific surface, and from Eq. (1) it is generally expressed as

$$\gamma = \frac{1}{A}\left(E + PV - TS - \sum_i N_i \mu_i\right). \quad (3)$$

If a system is modeled by a slab with two symmetric surfaces, each of which has the area A, then Eq. (3) becomes

$$\gamma = \frac{1}{2A}\left(E + PV - TS - \sum_i N_i \mu_i\right). \quad (4)$$

As discussed by Scheffler *et al.* [24, 25], the contributions from the PV and TS terms can be generally neglected, and then Eq. (4) is approximated as

$$\gamma = \frac{1}{2A}\left(E - \sum_i N_i \mu_i\right), \quad (5)$$

where E is directly obtained as the DFT total energy of the supercell containing the slab. Eq. (5) allows one to calculate the surface energy of a nonstoichiometric material surface and therefore has been applied to the studies of stabilities of various multicomponent material surfaces with different terminations [26, 27, 28, 29, 30, 31, 32, 33, 34, 35, 36, 37, 38, 39, 40, 41, 42]. Incidentally, for a single-component crystal surface, Eq. (5) reduces to the frequently-used well-known surface-energy formula

$$\gamma = \frac{E - N_1 \mu_1}{2A} = \frac{E - N\sigma_{\text{bulk}}}{2A}, \quad (6)$$

where the chemical potential μ_1 is often taken to be σ_{bulk}, the energy per atom in the bulk crystal, and $N_1 = N$ is the number of atoms in the slab.

In our DFT calculations for Li_2TiO_3 (001) surface, the system is modelled as a supercell containing a slab with two symmetric surfaces for any specific termination, as will described in Sec. IV. In this case, Eq. (5) can be rewritten as

$$\gamma = \frac{1}{2A}(E - N_{\text{Li}}\mu_{\text{Li}} - N_{\text{Ti}}\mu_{\text{Ti}} - N_{\text{O}}\mu_{\text{O}}), \quad (7)$$

where N_{Li}, N_{Ti}, and N_{O} are the numbers of Li, Ti, and O atoms in the slab; μ_{Li}, μ_{Ti}, and μ_{O} are the chemical potentials for the elements Li, Ti, and O, respectively. In general, $E = E(T, P, N_i)$ is a function of T, P, and N_i, while $\mu_i = \mu_i(T, P)$ is a function of T and P, where i denotes Li, Ti, or O.

If the surface is assumed to be in thermodynamic equilibrium with the surrounding Li_2TiO_3 bulk, then the sum of the three chemical potentials satisfies the chemical equilibrium condition

$$2\mu_{\mathrm{Li}} + \mu_{\mathrm{Ti}} + 3\mu_{\mathrm{O}} = \mu_{\mathrm{Li_2TiO_3,bulk}}, \tag{8}$$

where $\mu_{\mathrm{Li_2TiO_3,bulk}}$ is the chemical potential for bulk Li_2TiO_3 crystal. The requirement of Eq. (8) is from such fact that the bulk can exchange Li, Ti, or O atoms with the surface by, e.g., diffusion. From Eq. (8), only two in the three chemical potentials μ_{Li}, μ_{Ti}, and μ_{O} are independent. In general, the value of $\mu_{\mathrm{Li_2TiO_3,bulk}}$ depends on the experimental condition, but often approximated as the energy per unit formula of the bulk crystal at $T = 0$ K and $P = 0$ [24], $\sigma_{\mathrm{Li_2TiO_3}}$, which is directly obtained from DFT calculations.

The chemical-potential changes of Li, Ti, and O elements from bulk metal Li, bulk metal Ti, and O_2 gas to the surface system are

$$\Delta\mu_{\mathrm{Li}} = \mu_{\mathrm{Li}} - \mu_{\mathrm{Li,bulk}}, \ \Delta\mu_{\mathrm{Ti}} = \mu_{\mathrm{Ti}} - \mu_{\mathrm{Ti,bulk}}, \text{ and } \Delta\mu_{\mathrm{O}} = \mu_{\mathrm{O}} - \mu_{\mathrm{O,gas}}, \tag{9}$$

where $\mu_{\mathrm{Li,bulk}}$ ($\mu_{\mathrm{Ti,bulk}}$) is the chemical potential for bulk metal Li (Ti), and $\mu_{\mathrm{O,gas}}$ is the chemical potential for O_2 gas. In this work, we approximate $\mu_{\mathrm{Li,bulk}}$, $\mu_{\mathrm{Ti,bulk}}$, and $\mu_{\mathrm{O,gas}}$ as the per-atom energies σ_{Li}, σ_{Ti}, and σ_{O} for the bulk metal Li, bulk metal Ti, and O_2 gas, respectively, while σ_{Li}, σ_{Ti}, and σ_{O} are directly obtained from DFT calculations at $T = 0$ K and $P = 0$. Here note that the approximation $\mu_{\mathrm{O,gas}} \approx \sigma_{\mathrm{O}}$ is a reasonable choice for the chemical-potential range of interests [24], not implying O_2 is in a solid state at $T = 0$ K. From Eqs. (8) and (9), one has

$$2\Delta\mu_{\mathrm{Li}} + \Delta\mu_{\mathrm{Ti}} + 3\Delta\mu_{\mathrm{O}} = \Delta\mu_{\mathrm{f,Li_2TiO_3}}, \tag{10}$$

where $\Delta\mu_{\mathrm{f,Li_2TiO_3}} = \mu_{\mathrm{Li_2TiO_3,bulk}} - 2\mu_{\mathrm{Li,bulk}} - \mu_{\mathrm{Ti,bulk}} - 3\mu_{\mathrm{O,gas}}$ is the change of Gibbs free energy per unit formula for the formation of bulk Li_2TiO_3 from bulk metal Li, bulk metal Ti, and O_2 gas. Here it should be mentioned that $\Delta\mu_{\mathrm{f,M}}$, where M represents a multicomponent material, e.g., Li_2TiO_3, TiO_2, LiO_2, etc., is often called the formation energy of M from its constituent elements and compared with its corresponding standard formation enthalpy $\Delta H_{\mathrm{f,M}}$, which can be experimentally measured at the standard pressure of 100 kPa (101.325 kPa prior to 1982) and a specified temperature (e.g., usually 298.15 K and sometimes extrapolated to 0 K [43]). In this work, we take $\Delta\mu_{\mathrm{f,Li_2TiO_3}} \approx \sigma_{\mathrm{Li_2TiO_3}} - 2\sigma_{\mathrm{Li}} - \sigma_{\mathrm{Ti}} - 3\sigma_{\mathrm{O}} \equiv -\varepsilon$, which

can be obtained from our DFT calculations at $T = 0$ K and $P = 0$.

If we choose $\Delta\mu_{\mathrm{Ti}}$ and $\Delta\mu_{\mathrm{O}}$ as two independent variables and consider Eqs. (8) and (9), then Eq. (7) can be expressed as

$$\begin{aligned}\gamma = \frac{1}{2A}\Big[E - \frac{N_{\mathrm{Li}}}{2}\mu_{\mathrm{Li_2TiO_3,bulk}} + \Big(\frac{N_{\mathrm{Li}}}{2} - N_{\mathrm{Ti}}\Big)\left(\Delta\mu_{\mathrm{Ti}} + \mu_{\mathrm{Ti,bulk}}\right) \\ + \Big(\frac{3N_{\mathrm{Li}}}{2} - N_{\mathrm{O}}\Big)\left(\Delta\mu_{\mathrm{O}} + \mu_{\mathrm{O,gas}}\right)\Big] \\ \approx \frac{1}{2A}\Big[E - \frac{N_{\mathrm{Li}}}{2}\sigma_{\mathrm{Li_2TiO_3}} + \Big(\frac{N_{\mathrm{Li}}}{2} - N_{\mathrm{Ti}}\Big)\left(\Delta\mu_{\mathrm{Ti}} + \sigma_{\mathrm{Ti}}\right) \\ + \Big(\frac{3N_{\mathrm{Li}}}{2} - N_{\mathrm{O}}\Big)\left(\Delta\mu_{\mathrm{O}} + \sigma_{\mathrm{O}}\right)\Big]. \qquad (11)\end{aligned}$$

From Eq. (11), we can estimate the surface energy as a function of $\Delta\mu_{\mathrm{Ti}}$ and $\Delta\mu_{\mathrm{O}}$ for a given planar Li_2TiO_3 surface system. In experiments, these chemical potentials correspond to specific experimental environments (T and P) [24]. In this work, we consider the surface energies only within the bounds of the chemical potentials satisfying

$$-\varepsilon/2 \le \Delta\mu_{\mathrm{Li}} \le 0,\ -\varepsilon \le \Delta\mu_{\mathrm{Ti}} \le 0, \text{ and } -\varepsilon/3 \le \Delta\mu_{\mathrm{O}} \le 0. \qquad (12)$$

In Eq. (12), the upper bounds of $\Delta\mu_{\mathrm{Li}}$ and $\Delta\mu_{\mathrm{Ti}}$ guarantee that system does not decompose into bulk metal Li and bulk metal Ti, and O_2 gas, while the upper bound of $\Delta\mu_{\mathrm{O}}$ is a reasonable choice as an estimate of the truly accessible range [24]. The lower bounds of these inequality are determined by Eq. (10) and the upper bounds. The upper (lower) bound of $\Delta\mu_i$ is often called the "i-rich" ("i-poor") environment [24, 26] because a higher (lower) chemical potential corresponds to a higher (lower) concentration of the ith component.

In addition, we also consider the formation conditions of the binary oxides Li_2O and TiO_2. The formation energy from bulk metal Li and O_2 gas to bulk Li_2O is $\Delta\mu_{\mathrm{f,Li_2O}} = \mu_{\mathrm{Li_2O,bulk}} - 2\mu_{\mathrm{Li,bulk}} - \mu_{\mathrm{O,gas}}$, and it is $\Delta\mu_{\mathrm{f,TiO_2}} = \mu_{\mathrm{TiO_2,bulk}} - \mu_{\mathrm{Ti,bulk}} - 2\mu_{\mathrm{O,gas}}$ from bulk metal Ti and O_2 gas to bulk TiO_2. Here $\mu_{\mathrm{Li_2O,bulk}}$ and $\mu_{\mathrm{TiO_2,bulk}}$ can be approximately taken to be $\sigma_{\mathrm{Li_2O}}$ and $\sigma_{\mathrm{TiO_2}}$ (each of them is the energy per unit formula of the bulk crystal), which are directly obtained from DFT calculations at $T = 0$ K and $P = 0$ for bulk Li_2O and bulk Ti_2O, respectively. Thus, if the condition

$$2\Delta\mu_{\mathrm{Li}} + \Delta\mu_{\mathrm{O}} \le \Delta\mu_{\mathrm{f,Li_2O}} \qquad (13)$$

is satisfied, then the formation of bulk Li_2O is prohibited, and if the condition

$$\Delta\mu_{\mathrm{Ti}} + 2\Delta\mu_{\mathrm{O}} \le \Delta\mu_{\mathrm{f,TiO_2}} \qquad (14)$$

is satisfied, then the formation of bulk TiO_2 is prohibited.

III. DFT METHOD AND BENCHMARK CALCULATIONS

Our DFT calculations are performed using the plane-wave-based Vienna *ab initio* simulation package (VASP) code [44, 45]. The electron-core interactions with the pseudopotentials are generated from the projector augmented-wave (PAW) method [46] from the VASP group. The Perdew-Burke-Ernzerhof (PBE) generalized gradient approximation (GGA) [47] as the electronic exchange-correlation energy functional is implemented. The PBE GGA functional was already used to calculate bulk properties [48], defect formation energies [49], lithium diffusion [50], and tritium diffusion [51, 52] in Li_2TiO_3.

In our DFT calculations for the bulk Li_2TiO_3, we use a 2×1×1 supercell, as shown in Fig. 1. Based on our previous convergence tests [51], the energy cutoff for the plane-wave basis is taken to be 400 eV, and the G-centered $\boldsymbol{k}$ mesh is taken to be 3×2×2. The atoms of a system are always fully relaxed until the total force on any atom is less than 0.1 eV/nm. By optimizing the supercell geometry, we obtain the lattice constants: a = 0.5039 nm, b = 0.8744 nm, c = 0.9653 nm, and β = 100.2°; the interlayer spacings: $d_{\text{Li-O}}$ = 0.1270 nm and $d_{\text{O-LiTi}}$ = 0.1105 nm. These DFT geometric parameters are in good agreement with the experimental values in Sec. I. We also benchmark the band structure and density of states (DOS) of the bulk Li_2TiO_3, as plotted in Fig. 2. The corresponding band gap is 2.86 eV, which is reasonably consistent with the experimental value of 3.90 eV [53], as well as previous PBE value of 2.65 eV [20] and 3.20 eV [48]. The underestimation in band gap for most of semiconductors or insulators from PBE GGA calculations has been well-known and can have significant effects on excited-state properties but not the ground-state properties. The surface energies discussed in this work do not involve the excited-state properties and therefore PBE GGA is safe, as previously used in the calculations for other ground-state-related properties of Li_2TiO_3 [48, 49, 50, 51, 52].

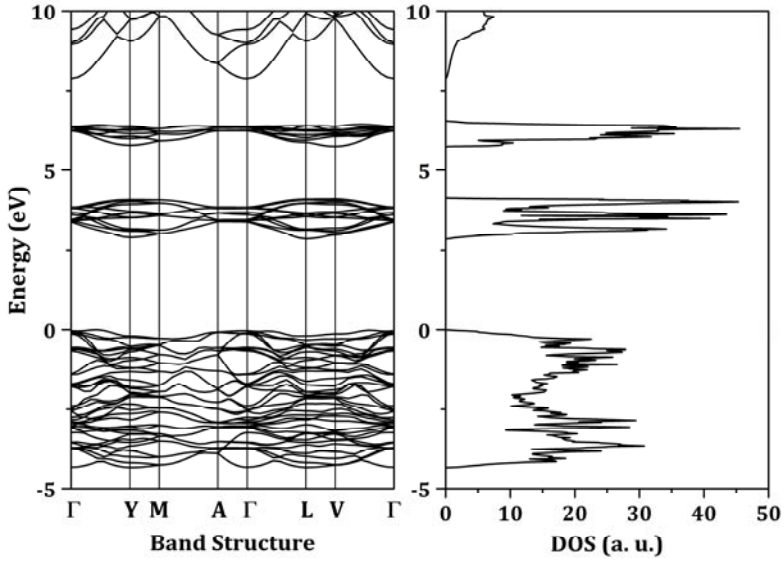

FIG. 2. Band structure (left) and DOS of the bulk Li_2TiO_3, from our DFT calculation. The Fermi energy level is set to be 0 eV on the vertical axis.

As described in Sec. II, to determine the relevant chemical potential ranges and build the surface phase diagram, one needs to know the involved formation energies. In Table I, we list the lattice constants and formation energies of bulk Li_2TiO_3, Li_2O, and TiO_2 from our DFT calculations. The comparison with experimental values shows good agreements. In the calculations for these formation energies, we use the values of σ_{Li}, σ_{Ti}, and σ_O from optimized bulk bcc Li, bulk hcp Ti, and O_2 molecule, respectively. The optimized lattice constant of bcc Li is $a = 0.3439$ nm (cf. experimental value 0.35092 nm at 20 °C [54]), while the optimized lattice constants of hcp Ti are 0.2922 and 0.4632 nm (cf. experimental values 0.295111 and 0.468433 nm at 25 °C [55]) for a and c, respectively. The optimized bond length of O_2 molecule in gas phase is 0.12343 nm (cf. experimental value 0.12074 nm [56]).

Table I. Lattice constants (a, b, and c in nm) and formation energies ($\Delta\mu_{f,M}$ in eV) of bulk Li_2TiO_3, Li_2O, and TiO_2 from our DFT calculations compared with experimental (exp.) lattice constants and formation enthalpies ($\Delta H_{f,M}$ in eV, at 0 K [43]).

		a	b	c	$\Delta\mu_{f,M}$ or $\Delta H_{f,M}$
Li_2TiO_3 (monoclinic)	DFT	0.5039	0.8744	0.9653	-17.388
	exp.	0.50623 [21]	0.87876 [21]	0.97533 [21]	-17.478 [43]
Li_2O (antifluorite)	DFT	0.4576			-6.165
	exp.	0.4573 [57]			-6.273 [43]
TiO_2 (rutile):	DFT	0.4607		0.2957	-9.912
	exp.	0.458666 [58]		0.295407 [58]	-9.876 [43]
TiO_2 (anatase):	DFT	0.3803		0.9497	-9.993
	exp.	0.378216 [58]		0.950226 [58]	

IV. PERFECT (DEFECT-FREE) (001) SURFACES

In our DFT calculation for any Li_2TiO_3 (001) slab, we always use a 2×1 supercell with a vacuum thickness of 1.5 nm and the $\boldsymbol{k}$ mesh is taken to be 3×2×1. All atoms in the slab are fully relaxed until the total force on any atom is less than 0.1 eV/nm. Specifically, to use Eq. (11) to calculate the surface energy of a nonstoichiometric surface termination, one needs to construct a symmetric slab with two exact same surfaces [41]. In addition, the thickness of the slab needs to be tested for convergence of surface energy.

After the above consideration, we initially construct 4 slabs before energy minimization for 4 possible types of perfect surface terminations with all atoms at their bulk lattice. The 4 slab models before relaxation are shown in Fig. 3, and the corresponding geometries after full relaxation are shown in Fig. 4. Because we always use the 2×1 supercell, 4 types of perfect surface terminations are denoted as $Li_{12/12}$ (or Li_1), $Li_{4/12}Ti_{8/12}$ (or $Li_{1/3}Ti_{2/3}$), $O_{12/12}$-LiTi (or O_1-LiTi), and $O_{12/12}$-Li (or O_1-Li) terminations, according to the notation rule mentioned in Sec. I. By comparing the fully-relaxed structures in Fig. 4 with their initial configurations in Fig. 3, the lateral (parallel to the surface) positions of surface atoms of Li_1, $Li_{1/3}Ti_{2/3}$, and O_1-LiTi terminations are not significantly changed, but there is a conservative reconstruction (i.e., the total number of atoms in the reconstructed surface is equal to that in bulk [59]) of the first two-monolayer surface atoms for the O_1-Li termination. For the relaxation along the direction vertical to the surface, in Table II

we list the interlayer spacing d_{ij} after full relaxation, where the integers i and j label the ith and jth single-atom layer (monolayer) from the top surface (with smaller integer) to the middle (with bigger integer) of the slab. We also list the relaxation percentage d_{ij} corresponding to the interlayer spacing d_{ij} with the definition of $\delta_{ij} = (d_{ij} - d_{ij}^{\circ})/d_{ij}^{\circ} \times 100\%$, where $d_{ij}^{\circ} = d_{\text{Li-O}}$ or $d_{\text{O-LiTi}}$ is the interlayer spacing before relaxation (e.g., that in Fig. 3). These interlayer spacings will be used to discuss the Li_2TiO_3 (001) surface structures in Sec. V.

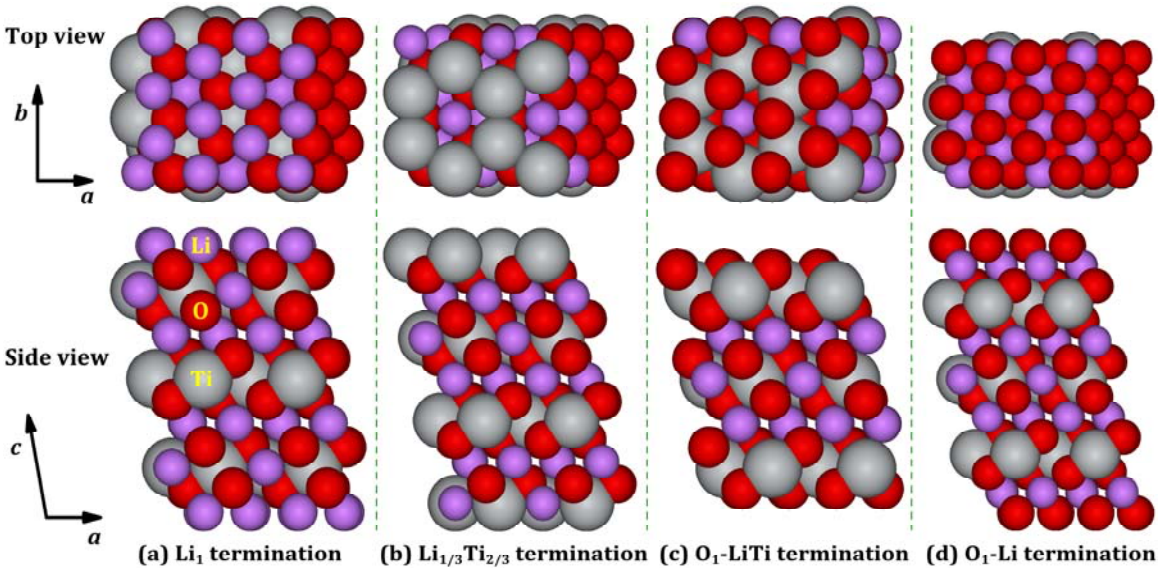

FIG. 3. Slab models before relaxation for 4 types of surface terminations of Li_2TiO_3 (001). (a) Li_1, (b) $Li_{1/3}Ti_{2/3}$, (c) O_1-LiTi, and (d) O_1-Li termination. The upper panel is top view, and the lower panel is side view.

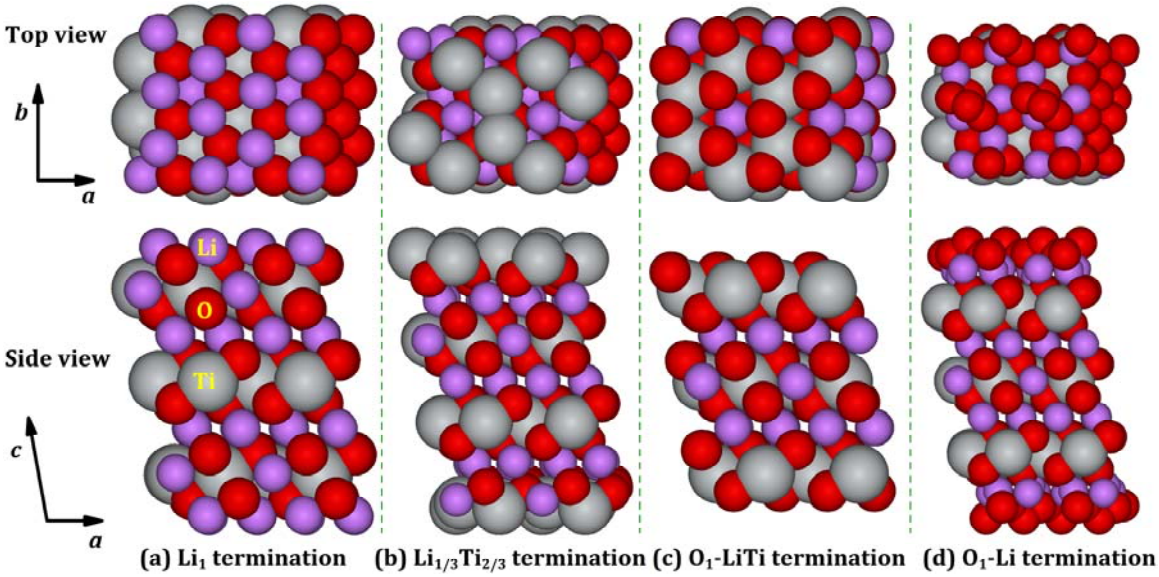

FIG. 4. Slab geometries after full relaxation for 4 types of surface terminations in Fig. 3. (a) Li_1, (b) $Li_{1/3}Ti_{2/3}$, (c) O_1-LiTi, and (d) O_1-Li termination. The upper panel is top view, and the lower panel is side view.

Table II. Interlayer spacings d_{ij} (in nm) and relaxation percentage d_{ij} of surface terminations from our DFT calculations.

Termination		d_{12}	d_{23}	d_{34}	d_{45}	δ_{12}	δ_{23}	δ_{34}	δ_{45}
Li_1	average[a]	0.0876	0.1282	0.1059	0.1341	-31.05%	16.01%	-4.15%	5.59%
	maximum[b]	0.0926	0.1369	0.1155	0.1400	-27.09%	23.89%	4.52%	10.24%
$Li_{1/3}Ti_{2/3}$	average	0.0945	0.1498	0.1198	0.1155	-14.49%	17.96%	-5.67%	4.52%
	maximum	0.1454	0.1829	0.1291	0.1182	31.58%	44.02%	1.65%	6.97%
O_1-LiTi	average	0.0874	0.1303	0.1229	0.1360	-20.87%	17.89%	-3.21%	7.08%
	maximum	0.0914	0.1397	0.1237	0.1369	-17.29%	26.43%	-2.60%	7.80%
O_1-Li	average	0.1377	0.1327	0.1132	0.1108	8.41%	4.45%	-2.49%	0.27%
	maximum	0.2176	0.1593	0.1233	0.1203	71.34%	25.43%	11.58%	8.87%
$Li_{1/3}$	average	0.0885	0.1107	0.1087	0.1302	-30.31%	0.18%	-1.63%	2.52%
	maximum	0.0886	0.1378	0.1237	0.1314	-30.23%	24.71%	11.95%	3.46%

[a] The interlayer spacing after taking an average value for all atoms of each monolayer.

[b] The interlayer spacing is calculated as the maximum vertical distance between two atoms in the *i*th and *j*th monolayer, respectively.

According to Eq. (11), the surface energy γ is a binary function of $\Delta\mu_{\mathrm{O}}$ and $\Delta\mu_{\mathrm{Ti}}$ for a given surface system, e.g., that in Fig. 4(a), 4(b), 4(c), or 4(d). Therefore, one can make a 3-dimensional (3D) plot of γ versus $\Delta\mu_{\mathrm{O}}$ and $\Delta\mu_{\mathrm{Ti}}$. For clarity, in Fig. 5 we only show the 2D plots of γ versus $\Delta\mu_{\mathrm{O}}$ at four selected $\Delta\mu_{\mathrm{Ti}}$ values, for each of which the surface energies of 4 types of Li_2TiO_3 (001) surface terminations are plotted. Also, in Fig. 5, only the ranges of chemical potentials satisfying Eqs. (10) and (12) are shown. From Fig. 5, we can see that there is always a chemical-potential region where O_1-Li, Li_1, or O_1-LiTi termination has the lowest surface energy and is hence most stable thermodynamically relative to other 3 terminations, but there is no such region for $Li_{1/3}Ti_{2/3}$ termination, i.e., the perfect $Li_{1/3}Ti_{2/3}$-terminated surface is unfavorable for any chemical-potential range. Here we also need to mention that the surface energy of a surface termination can be negative in some certain chemical-potential ranges [31, 32, 38], as seen in Fig. 5. From Eq. (1), a negative surface energy indicates that the surface phase of the material is more favorable in energy or more stable than the corresponding reservoir with the same chemical potentials, i.e., the process of the surface formation from the reservoir is exothermic.

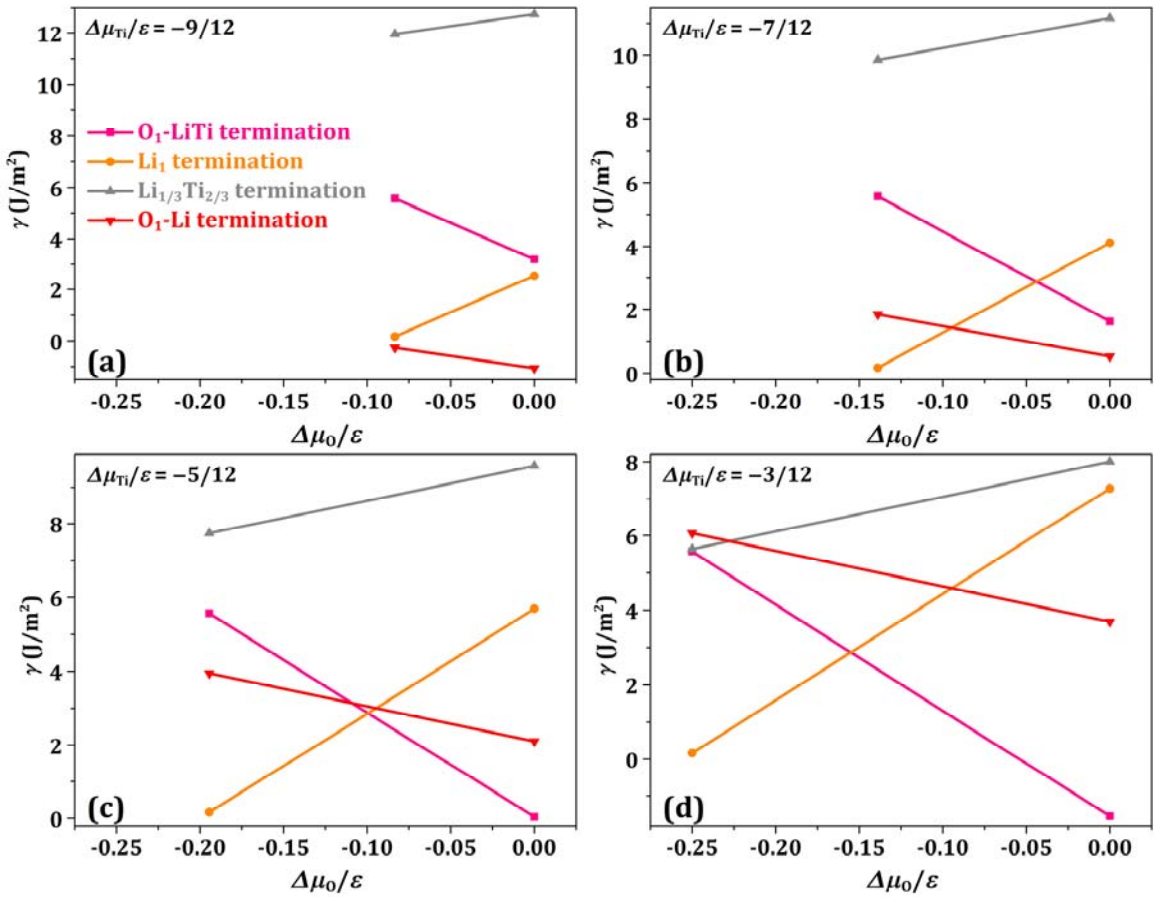

FIG. 5. Plots of surface energy γ versus $\Delta\mu_O$ (in units of ε) for 4 types of Li_2TiO_3 (001) surface terminations (corresponding to Fig. 4) at (a) $\Delta\mu_{Ti}/\varepsilon = -9/12$, (b) $\Delta\mu_{Ti}/\varepsilon = -7/12$, (c) $\Delta\mu_{Ti}/\varepsilon = -5/12$, and (d) $\Delta\mu_{Ti}/\varepsilon = -3/12$.

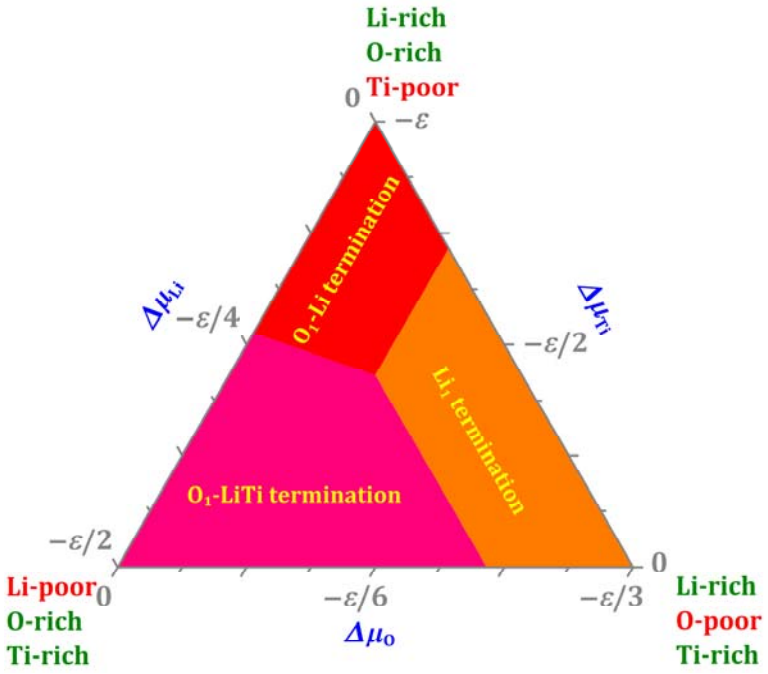

FIG. 6. Lowest-surface-energy ternary phase diagram for perfect Li_2TiO_3 (001) surface terminations. Each color indicates a chemical-potential region where any surface energy corresponding to a specific surface termination is lowest relative to other terminations.

To show a region corresponding to a most-stable surface termination, in Fig. 6 we plot the lowest-surface-energy ternary phase diagram for the perfect Li_2TiO_3 (001) surface terminations. In the O-poor (Li- and Ti-rich) region, the Li_1-terminated surface is most stable; in the Li-poor (O- and Ti-rich) region, the O_1-LiTi-terminated surface is most stable; in the Ti-poor (Li- and O-rich) region, the O_1-Li-terminated surface is most stable. In the ternary phase diagram, there is no any region where $Li_{1/3}Ti_{2/3}$-terminated surface is most stable, as analyzed above for Fig. 5.

V. VACANCY-DEFECTED (001) SURFACES

The STM experiments [19] show the structures of Li_2TiO_3 (001) surface can differ from the atomic arrangement of its bulk lattice, indicating the vacancies exist in the surface layer. In this section, we show our results of the energetics for vacancy-defected Li_2TiO_3 (001) surfaces.

We first explore the vacancy-defected Li_x-terminated surfaces. We only consider a 2×1 supercell in Fig. 3(a), where the number of Li atoms in the complete top Li monolayer of the supercell is 12. Then, the possible discrete coverages of Li on the O_1-LiTi-terminated subsurface are $n/12$, where n = 0, 1, 2, …, or 12 is the number of Li atoms in the top Li monolayer of the supercell. n = 1, 2, …, and 11 correspond to 11, 10, …, and 1 vacancy in the vacancy-defected Li top monolayer, respectively. n = 0

corresponds to the perfect O_1-LiTi-terminated subsurface and n = 12 corresponds to a perfect Li-terminated surface without vacancies. Note that if a larger supercell is chosen, the number of discrete coverages increases, e.g., for a 4×2 supercell, the possible coverages can be $n/48$ with n = 0, 1, 2, …, and 48. Obviously, in these coverages for the 4×2 supercell, there are 12 coverages with n = 4, 8, 16, …, and 48 repeating those for the 2×1 supercell. Although increasing the supercell size will lead to a denser coverage network, both larger system size and larger number of possible coverages (and therefore larger number of configurations of top Li atoms) will significantly increase the consumption of computation, while a denser coverage network does not bring more interested insights. Thus, we choose a reasonably small supercell size 2×1. As described below, the results from the 2×1 supercell have been sufficiently good to understand the vacancy-defected surfaces. Below, we use Li_x to denote a surface termination with the Li coverage at $x = n/12$. For a given coverage $x = n/12$, there are multiple configurations of Li atoms. In order to find the most favorable $Li_{n/12}$ termination, one needs to calculate the total energies of all possible configurations and compare these total energies.

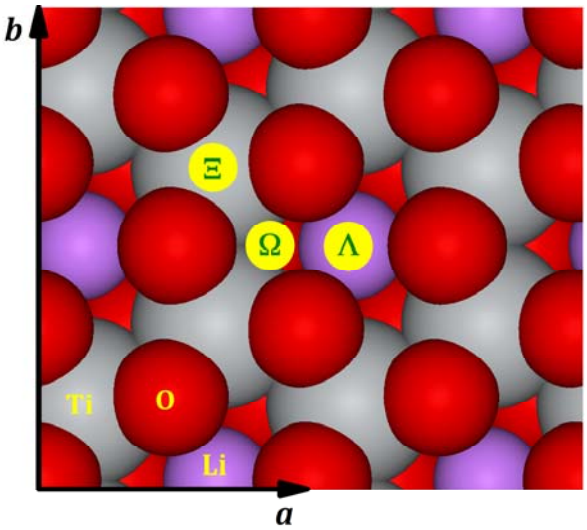

FIG. 7. Three most favorable adsorption sites L, W, and X for one Li atom on an O_1-LiTi-terminated subsurface.

By calculating the adsorption energies of one Li atom (n = 1 or x = 1/12) on the O_1-LiTi-terminated subsurface, we find that the most favorable adsorption site is the L site (see Fig. 7) with an adsorption energy of -6.62 eV. The second-most favorable adsorption site is the W site with an adsorption energy of -6.56 eV. It should be mentioned that there are three NN W sites with slightly different geometries (see Fig. 7), but our DFT results show the energy differences among them are less than 2 meV, so we do not distinguish them. The third-most favorable adsorption site is the X site with an adsorption energy of -6.36 eV. There are two NN X sites with slightly different geometries (see Fig. 7), but the energy difference between them is less than

2 meV, and then we do not distinguish them either. The adsorption energy of one Li adatom on the O_1-LiTi-terminated subsurface is calculated as

$$E_{\mathrm{ads}} = E_1 - E_{\mathrm{sub}} - E_{\mathrm{Li,gas}}, \tag{15}$$

where E_1 is half of the total energy of the slab with two symmetric subsurfaces (each of which absorbs one Li adatom), E_{sub} is half of the energy of the clean substrate with two symmetric O-LiTi-terminated subsurfaces on which no any Li atoms are absorbed, and $E_{\mathrm{Li,gas}}$ is the energy of one Li atom in gas phase. Because the adsorption energy at L site is significantly lower than the W and X site, we only consider the surface energy of the $Li_{1/12}$-terminated surface with the Li atom at L site (see Fig. 8(a)).

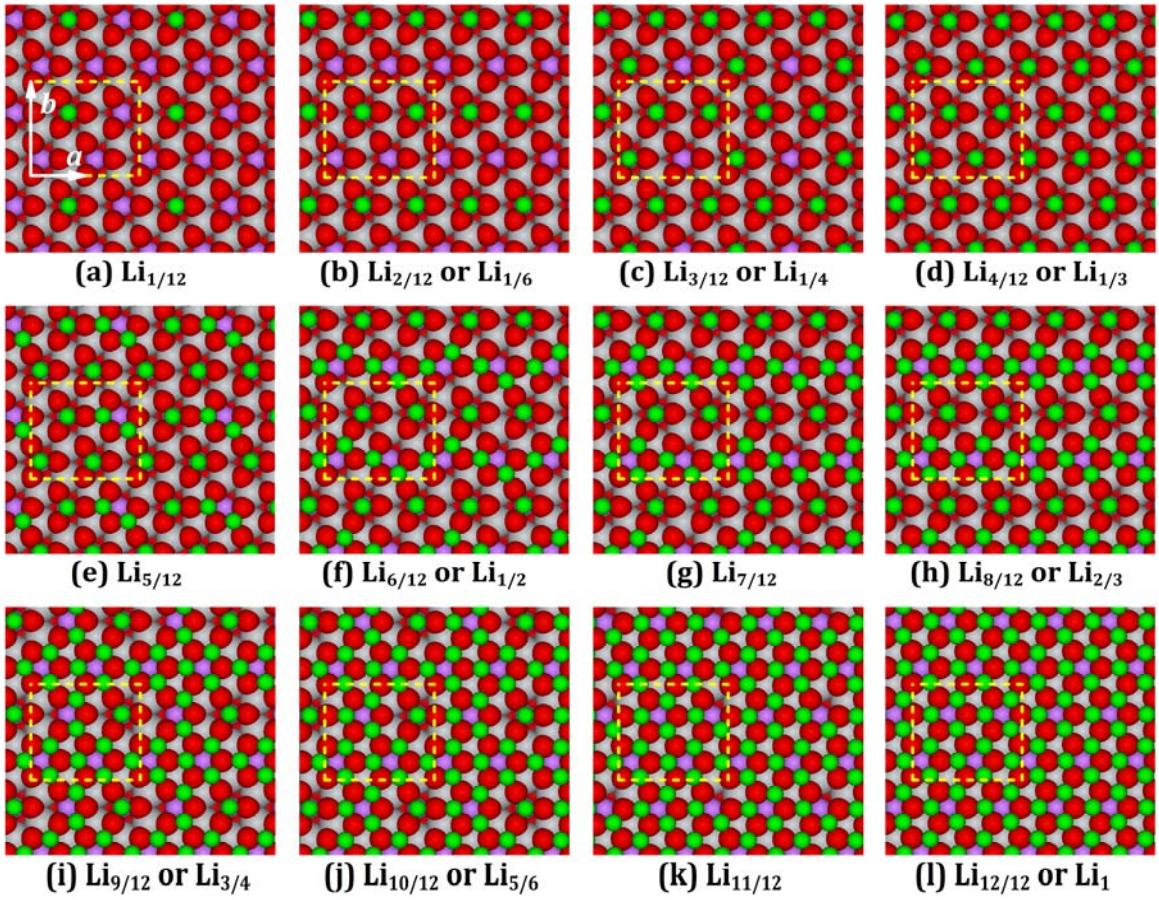

FIG. 8. Most favorable configuration of a $Li_{n/12}$-terminated surface by searching a limited number of configurations (see text). (a) n = 1, (b) n = 2, (c) n = 3, (d) n = 4, (e) n = 5, (f) n = 6, (g) n = 7, (h) n = 8, (i) n = 9, (j) n = 10, (k) n = 11, and (l) n = 12. For clarity, the top Li atoms are green-colored. The Li, O, and Ti atoms in sublayers are purple-, red-, and gray-colored, respectively. The yellow dashed frame represents the 2×1 supercell. The number of vacancies per supercell for a configuration with the coverage $x = n/12$ can be counted as $12 - n$, relative to the perfect Li termination in (l).

For two Li atoms (n = 2 or x = 2/12 = 1/6) on the O_1-LiTi-terminated subsurface, we selectively calculate the total energies of 12 configurations. For each configuration, two Li atoms are at two adsorption sites, and each adsorption site can be L, W, or X site. We find that the most favorable configuration in energy is that in Fig. 8(b), where two Li atoms are at two NN L sites. From these calculations, we also find that the total energy of any configuration including a X site is always significantly higher (0.5 eV at least) than any one not including a X site. The empirical-potential MD simulations of Azuma *et al*. also show that the Li atoms do not occupy the X sites [19]. Thus, it is safe that we do not generally consider X sites when calculating the configurations of $n > 2$ or $x > 1/6$ in the analysis below.

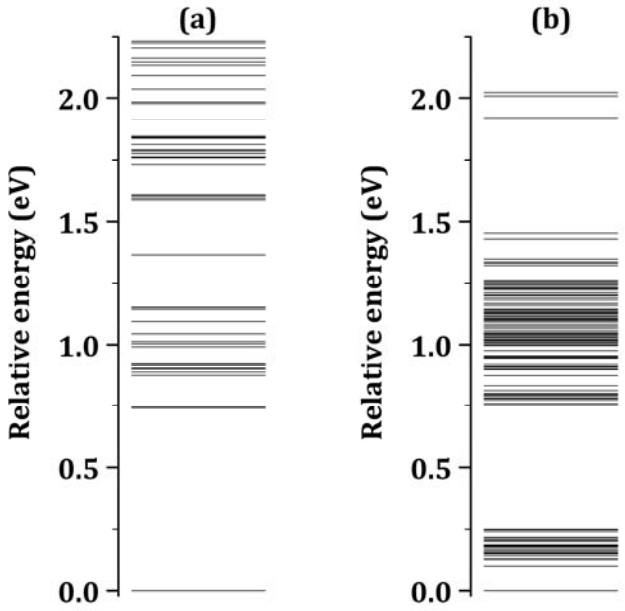

FIG. 9. The relative energies of (a) 48 symmetrically-different configurations for $Li_{1/3}$-terminated surface (the lowest level corresponds to Fig. 8(d)), and (b) 120 symmetrically-different configurations for $Li_{1/2}$-terminated surface (the lowest level corresponds to Fig. 8(f)).

Considering the above energies of configurations and the separations between two Li atoms for n = 2 or x = 1/6, it is expected that, for n = 3 or x = 3/12 = 1/4, the configurations in Fig. 8(c) is most favorable than other possible configurations. This is confirmed by selectively calculating 7 other configurations which have 0.28 to 2.31 eV higher energies than that in Fig. 8(c). Similarly, for n = 4, 5, 6, 7, 8, 9, 10, and 11, we selectively calculate 48, 3, 120, 3, 4, 4, 2, and 3 configurations, respectively. The most favorable configurations for these different Li coverages n from 1 to 12 are shown in Fig. 8. As an illustration, we plot the relative energies of 48 symmetrically-different configurations for n = 4 in Fig. 9(a), and 120 symmetrically-different configurations for n = 6 in Fig. 9(b). Each level in Fig. 9 is the energy value of a configuration relative to the lowest-energy configuration for a surface termination with a specific Li coverage x. For Fig. 9(a), x = 1/3 or n = 4, and for Fig. 9(b), x = 1/2 or n = 6. Note that the configuration space is large for an intermediate n value , e.g., for the 2×1 supercell, total number of sites is 16 (including 4 L sites and 12 W sites), and then there are $C_{16}^{4} = 1820$ and $C_{16}^{6} = 8008$ configurations for n = 4 and 6, respectively. In our calculations, we neither consider any occupation of two NN L and W sites on account of too high energies of such pairs due to too short separations nor the symmetrically same configurations. Therefore, the numbers of configurations to be considered are largely reduced. We select and calculate 48 and 120 symmetrically-different configurations for n = 4 and

6, as plotted in Figs. 9(a) and 9(b), respectively. As seen in Fig. 9(a), the first-lowest level is much lower than the second-lowest level, and the gap between them is 0.74 eV. The first-lowest level in Fig. 9(a) corresponds to the configuration in Fig. 8(d), where a periodic hexagonal-like pattern of top Li atoms is exhibited. The further discussion for this pattern will be presented in Sec. VI. In Fig. 9(b), the first-lowest level is 0.10 eV lower than the second-lowest level. The first-lowest level in Fig. 9(b) corresponds to the configuration in Fig. 8(f). This DFT result is not consistent with that obtained by Azuma *et al.*'s from an empirical-potential model, where the most favorable configuration (hereinafter referred to as the "EPM pattern") is shown in Fig. 8(b) in Ref. [19]. The EPM pattern actually corresponds to the 24th-lowest level with an energy of 0.246 eV relative to the first-lowest level in Fig. 9(b). This also indicates the failure of the empirical potential [17, 19] in predicting the stabilities of surface structures of Li_2TiO_3 crystal, at least in searching the lowest-energy structure for a specific Li coverage, e.g., $x = 1/2$ in Fig. 9(b). We will analyze this pattern again in Sec. VI.

In the above calculations, only 2D configurations of the top Li atoms are considered. To examine the possibility of the 3D configurations, we perform several types of calculations. Firstly, we initially construct a 4-Li-atom pyramid with 3 Li atoms at 3 NN W sites and the 4th Li atom on top of the base triangle. Such 4-Li-atom pyramids have three possible configurations, each of which corresponds to the 4th Li atom above a Li, O, or Ti atom of the sublayer (see Fig. 7). Fully relaxing these three 4-Li-atom pyramids obtains the energies of 1.85, 3.05, and 6.38 eV higher than those for the hexagonal-like 2D structure in Fig. 8(d). Secondly, we take one Li atom away from the perfect Li_1-terminated surface (Fig. 8(l)) (so that a vacancy is left) and position it at an adsorption site on top of Li monolayer with the vacancy. We only consider the configurations for which the Li adatom has a largest distant from the vacancy. For such configurations, there are three possible adsorption sites, each of which can be above a Li, O, or Ti atom of the sublayer, similar to the above 4-Li-atom pyramids. Fully relaxing these three configurations yields the energies of 1.94, 1.96, and 2.00 eV higher than those for the perfect 2D Li_1-terminated surface in Fig. 8(l). Similarly, we also select and calculate a 3D configuration with a 4-Li-atom pyramid for any of $x = 5/12$, $1/2$, $7/12$, $3/4$, and $5/6$, and find that these 3D structures have 3 to 6 eV higher energies than the corresponding 2D structures in Fig. 8. Thus, we do not consider the 3D structures for any Li_x terminations in this work.

In Fig. 10, we plot the surface energy γ versus $\Delta\mu_O$ for most favorable Li_x-terminated surfaces (corresponding to Fig. 8) at four selected $\Delta\mu_{Ti}$ values. The surface energies of 4 types of perfect Li_2TiO_3 (001) surface terminations (corresponding to Figs. 4 and 5) are also plotted in Fig. 10 for comparison. From Fig. 10, a chemical-potential region corresponding to the lowest surface energies can be

found for O_1-LiTi, Li_1, O_1-Li, $Li_{1/12}$, $Li_{1/6}$, $Li_{1/4}$, $Li_{1/3}$, $Li_{5/12}$, $Li_{1/2}$, or $Li_{5/6}$ termination, but no any region with the lowest surface energies corresponds to $Li_{1/3}Ti_{2/3}$, $Li_{7/12}$, $Li_{2/3}$, $Li_{3/4}$, or $Li_{11/12}$ termination.

To more clearly show the chemical-potential regions corresponding to most stable surface terminations, in Fig. 11 we plot the lowest-surface-energy ternary phase diagram for perfect Li_2TiO_3 (001) surface terminations and various most favorable Li_x-terminated surfaces. Compared with Fig. 6, the O-poor (Li- and Ti-rich), Li-poor (O- and Ti-rich), and Ti-poor (Li- and O-rich) regions in Fig. 11 still correspond to the most stable Li_1-, O_1-LiTi-, and O_1-Li-terminated surfaces, but the most stable Li_x terminations with different ribbon-like areas from $x = 1/12$ to $1/6$ to $1/4$ to $1/3$ to $5/12$ to $1/2$ to $5/6$ successively cover the middle part of the phase diagram from left to right, as indicated by various colors. These ribbon-like areas have different widths along the $\Delta\mu_O$ axis. Among them, the $Li_{1/2}$ region ($n = 6$, yellow-green) is widest, and the $Li_{1/3}$ region ($n = 4$, wine) has the second-largest width, while the $Li_{5/6}$ region ($n = 10$, black) is narrowest and actually reduced to a straight line (see Fig. 11). Note that there is no region corresponding to $Li_{1/3}Ti_{2/3}$, $Li_{7/12}$, $Li_{2/3}$, or $Li_{3/4}$ termination in the ternary phase diagram, as analyzed above for Fig. 10.

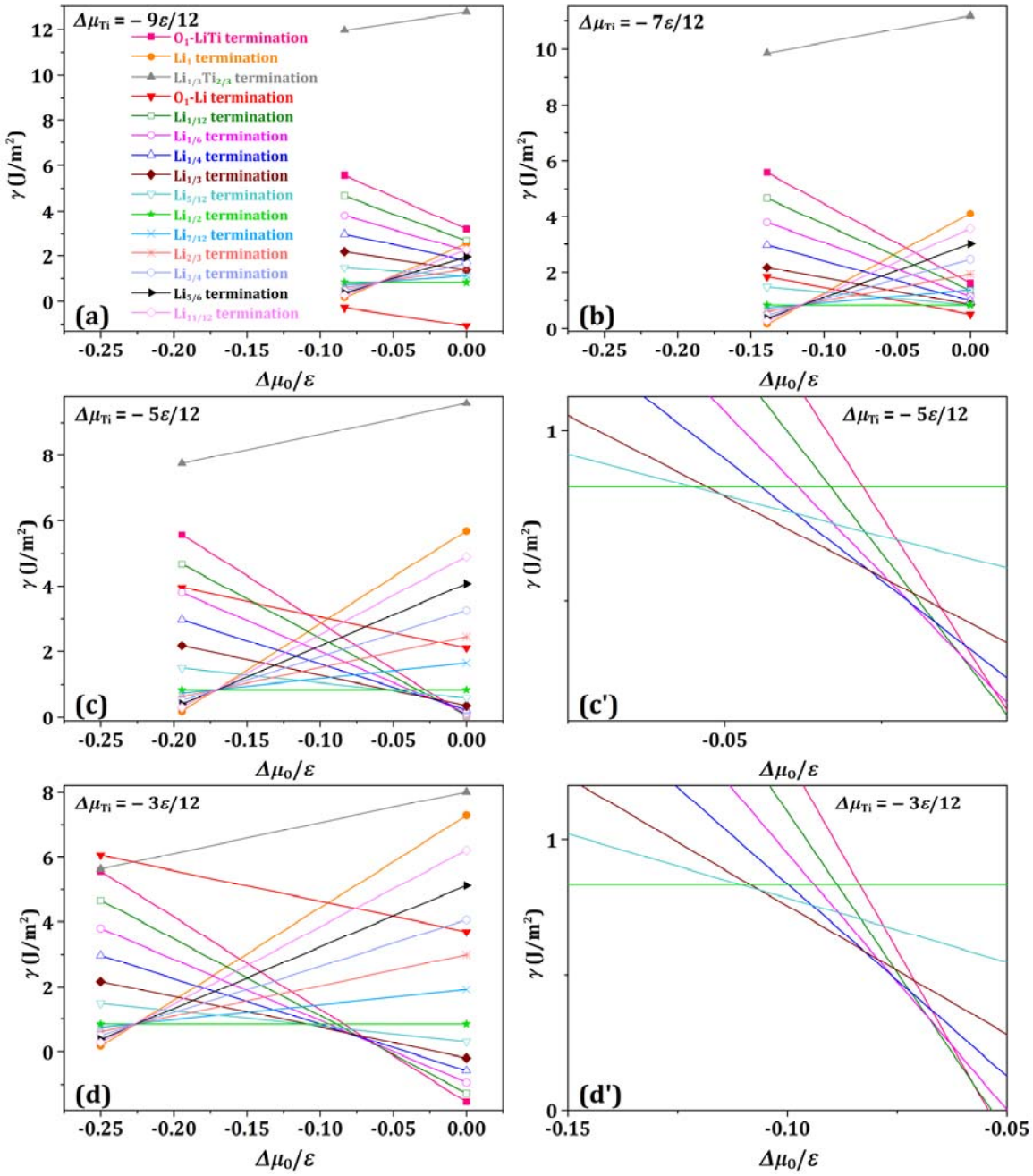

FIG. 10. Plots of surface energy γ versus $\Delta\mu_{\mathrm{O}}$ for most favorable $\mathrm{Li}_{n/12}$-terminated surfaces (corresponding to Fig. 8) at (a) $\Delta\mu_{\mathrm{Ti}}/\varepsilon = -9/12$, (b) $\Delta\mu_{\mathrm{Ti}}/\varepsilon = -7/12$, (c) $\Delta\mu_{\mathrm{Ti}}/\varepsilon = -5/12$, and (d) $\Delta\mu_{\mathrm{Ti}}/\varepsilon = -3/12$. (c') is a local enlargement of (c), and (d') is a local enlargement of (d). For comparison, the surface energies of 4 types of perfect $\mathrm{Li_2TiO_3}$ (001) surface terminations (corresponding to Figs. 4 and 5) are also plotted.

In Fig. 11, we also plot the formation boundaries of the binary bulk oxides Li_2O and TiO_2. Under the b1 line, the formation of bulk Li_2O is impossible, but forming bulk Li_2O is possible above the b1 line. Under the b2 (b3) line, the formation of bulk anatase (rutile) TiO_2 is possible, while forming bulk anatase (rutile) TiO_2 is impossible above the b2 (b3) line. Thus, the region where the formation of all these bulk oxides is impossible is only that narrow area between the b1 and b2 lines.

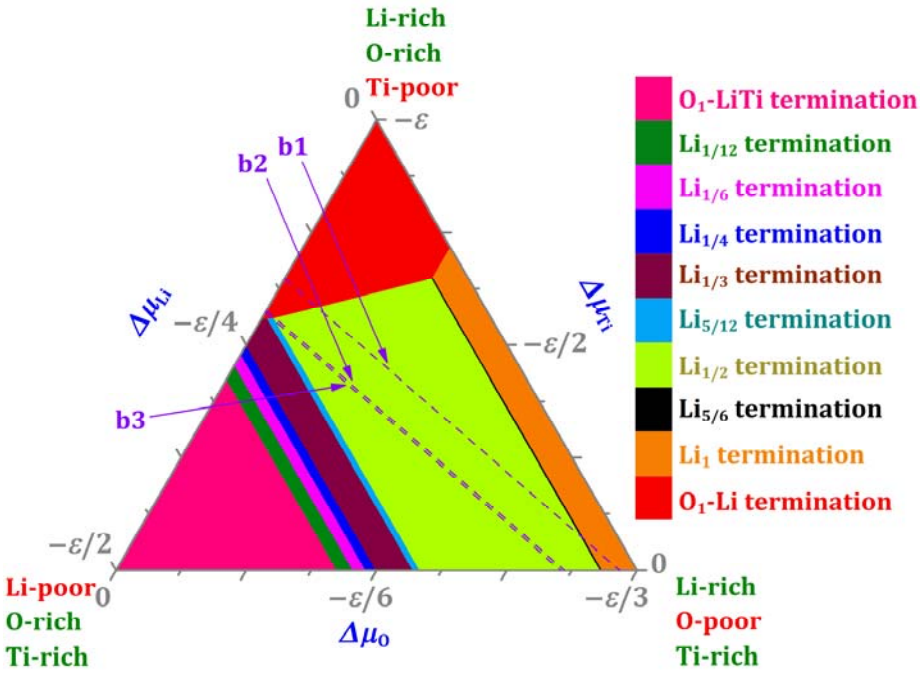

FIG. 11. Lowest-surface-energy ternary phase diagram for perfect Li_2TiO_3 (001) surface terminations (Fig. 6) plus vacancy-defected $Li_{n/12}$ terminations. Each color indicates a chemical-potential region where any surface energy corresponding to a specific surface termination is lowest relative to other terminations. The dashed lines b1, b2, and b3 indicate the formation boundaries of bulk Li_2O, bulk TiO_2 (anatase), and bulk TiO_2 (rutile), respectively.

For vacancy-defected O_x-Li-, Li_xTi_y-, or O_x-LiTi-terminated surfaces, in principle, one can perform similar calculations to the above vacancy-defected Li_x-terminated surfaces, but the number of configurations (including 2D and 3D) is huge even for a 2×1 supercell. Instead of calculating a large number of configurations, we selectively calculate several typical configurations of interest in light of available experimental observations [19], as will discussed in Sec. VI. These configurations before and after full relaxations are shown in Fig. 12, and the lowest-surface-energy ternary phase diagram after considering these configurations is shown in Fig. 13.

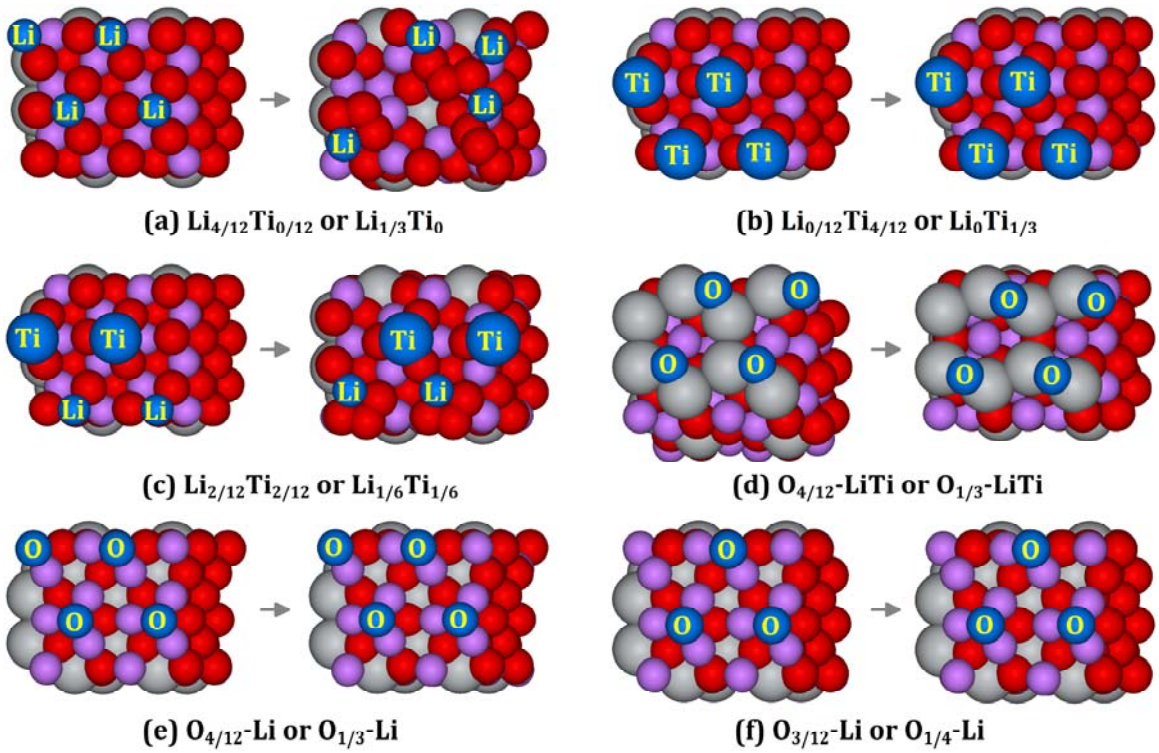

FIG. 12. Typical configurations for vacancy-defected Li_xTi_y-, O_x-LiTi-, and O_x-Li-terminated surfaces of Li_2TiO_3 (001). (a) $Li_{1/3}Ti_0$, (b) $Li_0Ti_{1/3}$, (c) $Li_{1/6}Ti_{1/6}$, (d) $O_{1/3}$-LiTi, (e) $O_{1/3}$-Li, and (f) $O_{1/4}$-Li termination. All atoms in a vacancy-defected terminated monolayer are blue-colored. The Li, O, and Ti atoms in sublayers are purple-, red-, and gray-colored, respectively. An arrow indicates the configurations before and after full relaxation from left to right.

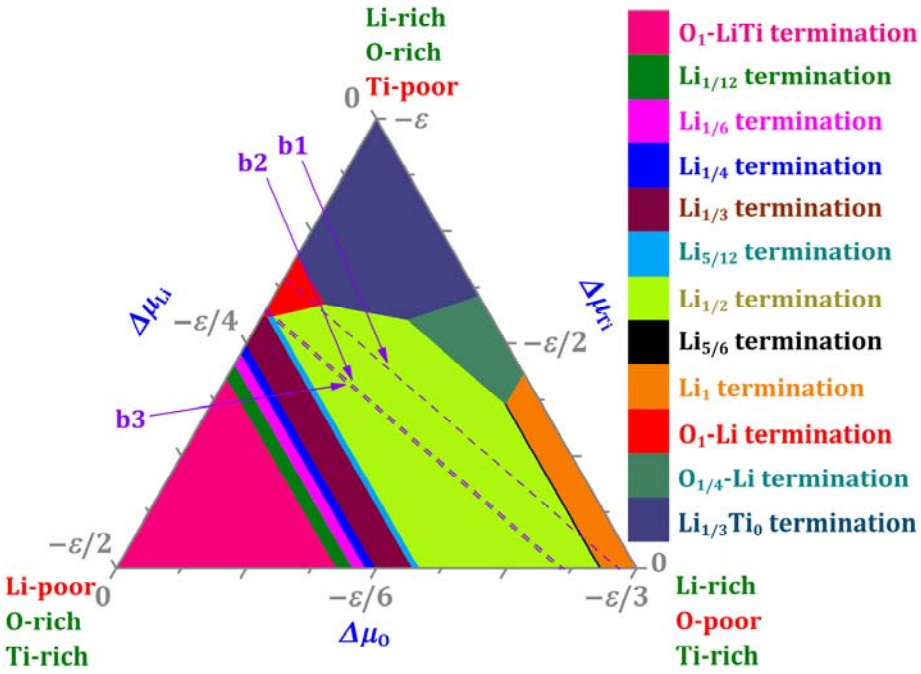

FIG. 13. Lowest-surface-energy ternary phase diagram for perfect Li_2TiO_3 (001) surface terminations and vacancy-defected $Li_{n/12}$ terminations (Fig. 11) plus vacancy-defected Li_xTi_y-, O_x-LiTi-, and O_x-Li-terminated surfaces in Fig. 12.

VI. DISCUSSION

The step heights of terraces on Li_2TiO_3 (001) surface observed from experimental STM images are around 0.25 nm [19], which is approximately equivalent to a two-monolayer height (see Fig. 1(b) and Table II). Here we assume that the sum $(d_{12} + d_{23})$ of two topmost interlayer spacings for any surface termination does not significantly change relatively to the bulk value, as listed in Table II. Thus, two surfaces of the upper and lower terraces of a step can be either O_x-LiTi- and O_x-Li-terminated (i.e., both terminations are oxygen anion monolayers), or Li_x- and Li_xTi_y-terminated (i.e., two terminations are lithium and lithium-titanium cation monolayers, respectively), and it is possible that any monolayer as a surface termination can be vacancy-defected and reconstructed [19].

In addition to the step heights, an interesting and helpful factor to determine the possible structure of the surface termination can be the observed hexagonal-like patterns with a periodicity of about 0.5 nm [60] from the experimental STM images. From the lowest-surface-energy ternary phase diagram in Fig. 11, a chemical-potential region (wine-colored), where a $Li_{1/3}$ termination is most stable, can be found. The configuration of this $Li_{1/3}$ termination is actually a non-conservative reconstruction (i.e., the total number of atoms in the reconstructed surface is unequal to that in bulk [59] because it is vacancy-defected), as shown in Fig. 8(d) or 12(a), featured by a triangular lattice with one side length $l_1 = 0.5039$

nm and other two side lengths $l_2 = 0.5046$ nm from our DFT calculation. The l_1 and l_2 values, which can be obtained from previous experimental lattice constants [21], are 0.5062 and 0.5071 nm, respectively. Because $l_1 \approx l_2$, the pattern looks hexagonal-like. If there are no more configurations which have even lower surface energies than those within the wine-colored chemical-potential region in Fig. 11, the $Li_{1/3}$ termination should be globally most stable, i.e., a hexagonal-like pattern should be observed, as revealed by our DFT-simulated STM image in Fig. 12(b), when the experimental condition satisfies this chemical-potential range. However, the chemical potentials corresponding to the experiments are not available, and thus we need to check more possibilities. Here we also should mention that our DFT-simulated STM image is obtained within the Tersoff-Hamann approximation [61], and we take a reasonable sample bias of 3.7 V under the constant current mode by considering the value of 3.0 V used in experiment [19] and the energy gap of 2.86 eV from our DFT calculations in Fig. 2.

Let us first examine the EPM pattern (a $Li_{1/2}$ termination) suggested in Ref. [19]. On the one hand, from our DFT calculations, the configuration corresponding to the EPM pattern has a DFT energy of 0.246 eV higher than the configuration in Fig. 8(f) and is more unfavorable than 23 configurations for the $Li_{1/2}$ terminations, as analyzed in Sec. V. Also note that the configuration in Fig. 8(f) does not correspond to the above hexagonal-like pattern. On the other hand, using the configuration (Fig. 12(c)) corresponding to the EPM pattern, we cannot obtain any DFT-simulated STM image which looks hexagonal-like, as seen in Fig. 12(d). Thus, we do not suggest $Li_{1/2}$ termination to be the hexagonal-like pattern observed in the experimental STM images.

Then we examine the possible structures which look like a hexagonal pattern before geometric optimization for vacancy-defected Li_xTi_y terminations. From the bonding analysis for possible adsorption sites for a Li or Ti atom on the O_1-Li-terminated subsurface, we choose three most possible configurations shown in Figs. 12(a), 12(b), and 12(c). Our DFT calculations show that the configuration (a $Li_0Ti_{1/3}$ termination) in Fig. 12(b) has relatively high surface energies (with a range from 0.76 to 3.92 J/m^2) and no any lowest-surface-energy region appearing within the ternary phase diagram in Fig. 13. For both $Li_{1/3}Ti_0$ (Fig. 12(a)) and $Li_{1/6}Ti_{1/6}$ (Fig. 12(c)) terminations, the configurations after full relaxations become away from a hexagonal-like pattern. Thus, one should exclude these vacancy-defected Li_xTi_y terminations for the hexagonal-like pattern.

Let us examine possible O_x-LiTi terminations. We choose a typical configuration ($O_{4/12}$-LiTi or $O_{1/3}$-LiTi termination) in Fig. 12(d), which has a hexagonal-like structure. Our DFT calculations show that this configuration after full relaxation has relatively high surface energies (with a range from 0.99 to 10.46 J/m^2) and no any lowest-surface-energy region appearing within the ternary phase diagram in Fig. 13.

By checking the bonding details of possible adsorption sites for an O atom on the $Li_{1/3}Ti_{2/3}$-terminated subsurface, we expect that other $O_{1/3}$-LiTi terminations are not more favorable than that in Fig. 12(d). Then, one should also exclude any $O_{1/3}$-LiTi termination.

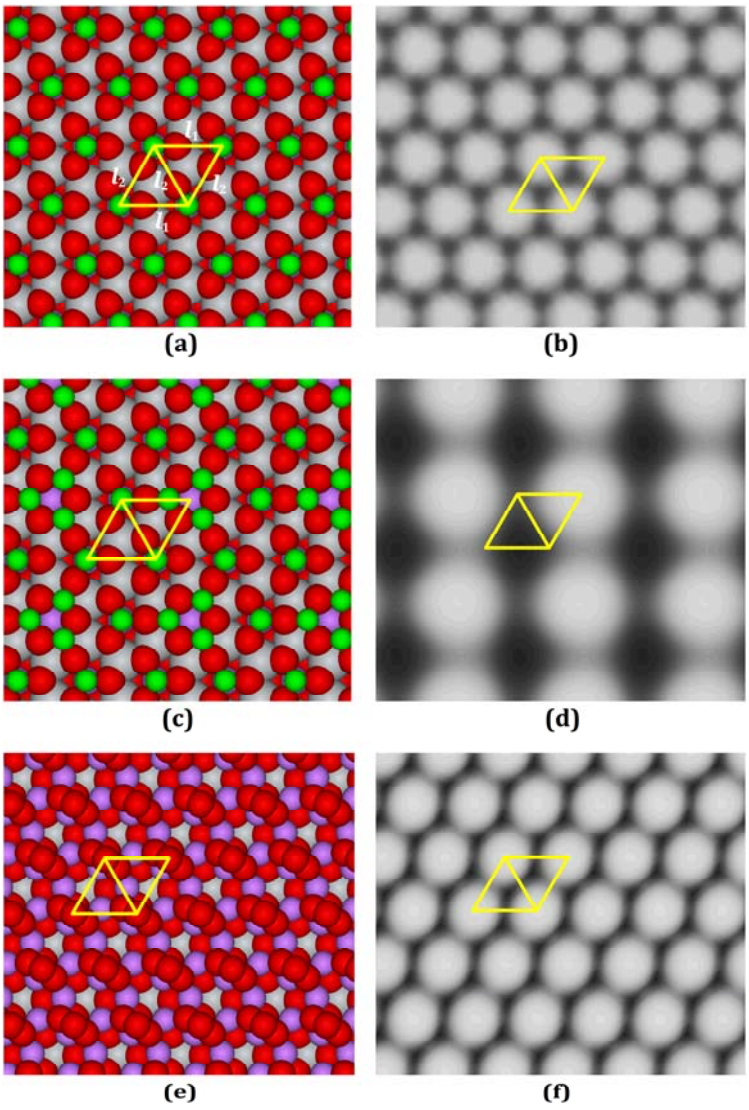

FIG. 14. (a) Fully-relaxed geometry of most favorable $Li_{1/3}$-terminated surface, which is the same as Fig. 8(d). The periodicity of the pattern is indicated by two triangles with the side lengths l_1 and l_2. (b) DFT-simulated STM image corresponding to (a). (c) Fully-relaxed geometry of a $Li_{1/3}$-terminated surface which is the EPM pattern in Fig. 8(b) in Ref. [19]. (d) DFT-simulated STM image corresponding to (c). (e) Fully-relaxed geometry of O-Li-terminated surface, which is the same as Fig. 4(d). (f) DFT-simulated STM image corresponding to (e). In (a) and (c), the top Li atoms are green-colored. The Li, O, and Ti atoms in (e) or in sublayers

of (a) and (c) are purple-, red-, and gray-colored, respectively. For (b), (d), or (f), the sample bias is set to be 3.7 V at a constant electron density of 10^{-8} nm^{-3} under the constant current mode.

Now we examine O_x-Li terminations. It is indeed that the periodicity of the conservative reconstruction after full relaxation of the perfect O_1-Li termination (Fig. 4(d) or Fig. 12(e)) is hexagonal-like, but the pattern, as displayed by the DFT-simulated STM image in Fig. 12(f), is rather anisotropic in contrast to the Fig. 12(b). On the other hand, the region (red-colored) corresponding to this termination in the lowest-surface-energy ternary phase diagram largely shrinks when the vacancy-defected surface terminations are taken into account: from Fig. 6 to Fig. 11, the red-colored region is partly replaced by the yellow-green color representing the $Li_{1/2}$ termination in Fig. 8(f); from Fig. 11 to Fig. 14, most of the red-colored region is further occupied by the dark-blue color representing the $Li_{1/3}Ti_0$ termination in Fig. 12(a). Thus, only a small red region at the most is left finally. From this analysis, we expect that the reconstructed O_1-Li termination has few opportunities as the experimentally-observed hexagonal-like pattern because the chemical-potential region is too small so that satisfying such conditions might be difficult experimentally, although it cannot be excluded completely. We also consider an $O_{1/3}$-Li termination in Fig. 12(e) as a possible hexagonal-like structure, but the no any lowest-surface-energy region corresponding to it appears within the ternary phase diagram in Fig. 13, and therefore this termination is excluded too.

Based on the above analysis, we conclude that the $Li_{1/3}$ termination in Fig. 8(d) is the most likely structure corresponding to the hexagonal-like pattern observed in experimental STM images [19]. Here we must emphasize that, for a given chemical-potential pair $\Delta\mu_{\mathrm{Ti}}$ and $\Delta\mu_{\mathrm{O}}$, more stable structures than the configurations considered in the above analysis are still possible, and the lowest-surface-energy ternary phase diagram will be thereby updated if a more stable structure exists. For example, from our DFT calculations, the surface energies of an $O_{1/4}$-Li termination in Fig. 12(f) are lower than the Li_1, $Li_{5/6}$, and, $Li_{1/2}$ terminations within a chemical-potential range, and then the region corresponding to this chemical-potential range in the phase diagram is updated from the orange, black, and yellow-green colors in Fig. 11 to the blue-green color in Fig. 13. As mentioned in Sec. V, exhausting all 2D and 3D configurations is difficult or impossible computationally due to a huge number of entire configurations. Nevertheless, given the hexagonal-like pattern observed in experiment, we expect that the possible configurations selected in the above analysis are enough for the purpose of interpreting such pattern.

In Fig. 11 or 13, we also plot the formation boundaries of bulk Li_2O, bulk TiO_2 (anatase), and bulk TiO_2 (rutile) as the dashed lines b1, b2, and b3, respectively. As stated in Sec. V, the formation of bulk TiO_2 is possible under the b2 line, while the

whole wine-colored region (the $Li_{1/3}$ termination) is under the b2 line. This indicates that bulk TiO_2 can form under the same chemical-potential environment as that for the $Li_{1/3}$ termination. The domination of bulk TiO_2 formation or appearance of the $Li_{1/3}$ termination should depend on the availabilities of Ti, O, and Li in the environment at the surface. For example, an environment of insufficient Ti and/or O will lead to the appearance of the $Li_{1/3}$ termination (i.e., the hexagonal-like pattern), while insufficient Li (i.e., relatively-plentiful Ti and O) will result in the precipitation of TiO_2 on the surface. Similarly, changing chemical potentials into the region above the b1 line and under an environment of relatively-plentiful Li and O, the precipitation of Li_2O will appear on the surface.

In Azuma *et al.*'s experiments [19], the annealing at 1200 K does not lead to ordered domains. This may be attributed to the corresponding chemical potentials out of the wine-colored region in the phase diagram in Fig. 13. In contrast, that the experimental STM images for the annealing at 1400 K exhibit the hexagonal-like pattern [19] is because the corresponding chemical potentials are within the wine-colored region in the phase diagram in Fig. 13. Further annealing at around 1400 K (even though the chemical potentials do not significantly change) may cause an environment of relatively-plentiful Ti and O (e.g., by diffusion of atoms along the surface, dewetting, or desorption-adsorption process of atoms from surface defects or other non-(001) facets of the Li_2TiO_3 sample at such high temperature) so that the precipitation of TiO_2 develops on the terraces and consequently the ordered domains with hexagonal-like pattern disappear finally, as observed in experiments [19]. It is also possible that the further annealing around 1400 K leads to the significantly-changed chemical potentials to be out of the wine-colored region in the phase diagram in Fig. 13. This also causes the disappearance of the ordered domains because the chemical potentials out of the wine-colored region do not correspond to the hexagonal-like pattern, as analyzed in Sec. V. As far as this is concerned, due to insufficient information from the experiments, it is difficult to distinguish that the chemical potentials are significantly changes or remain unchanged during the further annealing around 1400 K.

During annealing at 1400 K, the experimental STM images show the straight step edges separate with the terrace widths of several tens of nanometers and step heights around 0.25 nm [19]. Based on the bulk values of interlayer spacings as well as optimized values listed in Table II for various surface terminations, two surfaces of the upper and lower terraces of a step can be either O_x-LiTi- and O_x-Li-terminated, or Li_x- and Li_xTi_y-terminated, as discussed at the beginning of this section. Because our above analysis shows that a hexagonal-like pattern appearing on a terrace in the experimental STM images is likely the $Li_{1/3}$ termination in Fig. 8(d) or 14(a), the two terraces connecting this terrace should be Li_xTi_y-terminated surfaces, on which there should be no ordered hexagonal-like patterns observed, i.e., the appearance and

disappearance of the hexagonal-like patterns are alternative when crossing the steps. This theoretical prediction needs further confirmation in the future experimental studies on the Li_2TiO_3 (001) surface.

VII. SUMMARY

We have performed extensive first-principles DFT calculations for surface energies of various perfect (defect-free) and vacancy-defected Li_2TiO_3 (001) surface terminations and obtained the corresponding lowest-surface-energy ternary phase diagrams. For four possible perfect surface terminations, we find that Li_1-, O_1-Li-, or O_1-LiTi-terminated (001) surfaces can be most stable in a limited chemical-potential region, while $Li_{1/3}Ti_{2/3}$-terminated (001) surface is always unfavorable relative to other three terminations. By calculating the energies of different configurations for a vacancy-defected Li_x termination with a given coverage x of Li, we obtain the energetically-most-favorable structure and the corresponding surface energy. We also selectively consider Li_xTi_y-, O_x-Li-, and O_x-LiTi-terminated (001) surfaces. From the ternary phase diagram as well as our DFT-simulated STM images, we find that a $Li_{1/3}$-terminated surface most likely corresponds to the ordered hexagonal-like pattern observed in previous STM experiments [19]. The ternary phase diagram also shows that the oxides can simultaneously form with specific surface terminations and consequently rough the surface. In addition, we find that the energetically-most-favorable structure in $Li_{1/2}$-terminated surfaces from our DFT calculations is not consistent with previous result from an empirical-potential model [19]. Finally, from our DFT results, we predict that, crossing the steps of Li_2TiO_3 (001) surface, the alternative domains with and without the hexagonal-like pattern can appear under an appropriate experimental condition, e.g., annealing at 1400 K, and the future further experimental confirmation on this is needed.

This work provides an atomistic-level understanding for Li_2TiO_3 (001) surfaces from DFT calculations, and the obtained surface energy phase diagrams can be helpful for further Li_2TiO_3 (001)-associated studies, e.g., adsorption, diffusion, desorption, or reaction of hydrogen isotopes, hydroxyl groups, water molecules, etc. The method in this work can be applied for other similar three-component systems.

ACKNOWLEDGMENTS

Y. J., Y. S., J. Q., Z. L. and T. L. acknowledge support from the National Magnetic Confinement Fusion Science Program (2014GB125002) and the National Natural Science Foundation of the People's Republic of China (number11775152). Y. H. was supported for this work by the U. S. Department of Energy (USDOE), Office of Science, Basic Energy Sciences, Materials Sciences and Engineering Division. His work was performed at Ames Laboratory which is operated by Iowa State University under Contract No. DE-AC02-07CH111358. The DFT calculations partly used resources of

the National Energy Research Scientific Computing Center (NERSC), a U.S. DOE Office of Science User Facility operated under Contract No. DE-AC02-05CH11231, and also partly used the Extreme Science and Engineering Discovery Environment (XSEDE), which is supported by National Science Foundation grant number ACI-1548562. Finally, we also thank James W. Evans for his critical reading and helpful suggestions.

References:

[1] P. Gierszewski, Review of Properties of Lithium Metatitanate. Fusion Eng. Des. **39-40**, 739 (1998).

[2] C. E. Johnson, K. Noda, and N. Roux, Ceramic breeder materials: Status and needs, J. Nucl. Mater. **258-263**, 140 (1998).

[3] A. Ying, M. Akiba, L. V. Boccaccini, S. Casadio, G. Dell'Orco, M. Enoeda, K. Hayashi, J. B. Hegeman, R. Knitter, J. van der Laan, J. D. Lulewicz, and Z. Y. Wen, Status and perspective of the R&D on ceramic breeder materials for testing in ITER, J. Nucl. Mater. **367-370**, 1281 (2007).

[4] P. Garin, E. Diegele, R. Heidinger, A. Ibarra, S. Jitsukawa, H. Kimura, A. Möslang, T. Muroga, T. Nishitani, Y. Poitevin, M. Sugimoto, and M. Zmitko, IFMIF specifications from the users point of view, Fusion Eng. Des. **86**, 611 (2011).

[5] R. Knitter, P. Chaudhuri, Y. J. Feng, T. Hoshino, and I. K. Yu, Recent developments of solid breeder fabrication, J. Nucl. Mater. **442**, S420 (2013).

[6] S. Konishi, M. Enoeda, M. Nakamichi, T. Hoshino, A. Ying, S. Sharafat, and S. Smolentsev, Functional materials for breeding blankets-status and developments, Nucl. Fusion **57**, 092014 (2017).

[7] V. Chauvaut, M. Cassir, and Y. Denos, Behavior of titanium species in molten Li_2CO_3–Na_2CO_3 and Li_2CO_3–K_2CO_3 under anodic and cathodic conditions. I – Thermodynamic predictions at 550–750°C, Electrochim. Acta **43**, 1991 (1998).

[8] V. Chauvaut and M. Cassir, Behaviour of titanium species in molten Li_2CO_3 + Na_2CO_3 and Li_2CO_3 + K_2CO_3 in the anodic conditions used in molten carbonate fuel cells: II. Electrochemical intercalation of Li^+ in Li_2TiO_3 at 600 and 650°C, J. Electroanal. Chem. **474**, 9 (1999).

[9] L. Zhang, X. Wang, H. Noguchi, M. Yoshio, K. Takada, and T. Sasaki, Electrochemical and ex situ XRD investigations on $(1-x)LiNiO_2{\cdot}xLi_2TiO_3$ ($0.05 \le x \le 0.5$), Electrochim. Acta **49**, 3305 (2004).

[10] Y. Wang, A. Zhou, X. Dai, L. Feng, J. Li, and J. Li, Solid-state synthesis of submicron-sized $Li_4Ti_5O_{12}/Li_2TiO_3$ composites with rich grain boundaries for lithium ion batteries, J. Power Sources **266**, 114 (2014).

[11] Z. Zhang, G. Hu, Y. Cao, J. Duan, K. Du, and Z. Peng, Enhanced electrochemical performance of nano $LiMnPO_4$ with multifunctional surface co-coating of Li_2TiO_3 and carbon, Solid State Ion. **283**, 115 (2015).

[12] H. S. Bhatti, D. H. Anjum, S. Ullah, B. Ahmed, A. Habib, A. Karim, and S. K. Hasanain, Electrochemical characteristics and Li^+ ion intercalation kinetics of dual-phase $Li_4Ti_5O_{12}/Li_2TiO_3$ composite in the voltage range 0−3 V, J. Phys. Chem. C **120**, 9553 (2016).

[13] A. Sayyadi-Shahraki, E. Taheri-Nassaj, S. A. Hassanzadeh-Tabrizi, and H. Barzegar-Bafrooei, A new temperature stable microwave dielectric ceramic with low-sintering temperature in Li_2TiO_3–$Li_2Zn_3Ti_4O_{12}$ system, J. Alloys Compd. **597**, 161 (2014).

[14] A. L. Narayana, M. Dhananjaya, N. G. Prakash, O. M. Hussain, and C. M. Julien, Nanocrystalline Li_2TiO_3 electrodes for supercapattery application, Ionics **23**, 3419 (2017).

[15] C. E. Johnson, Tritium behavior in lithium ceramics, J. Nucl. Mater. **270**, 212 (1999).

[16] T. Kinjyo, M. Nishikawa, M. Enoeda, and S. Fukada, Tritium diffusivity in crystal grain of Li_2TiO_3 and tritium release behavior under several purge gas conditions, Fusion Eng. Des. **83**, 580 (2008).

[17] M. Vijayakumar, S. Kerisit, Z. Yang, G. L. Graff, J. Liu, J. A. Sears, S. D. Burton, K. M. Rosso, and J. Hu, Combined ^{6,7}Li NMR and molecular dynamics study of Li diffusion in Li_2TiO_3, J. Phys. Chem. C **113**, 20108 (2009).

[18] D. Zhu, T. Oda, Y. Shono, and S. Tanaka, Release behavior of hydrogen isotopes thermally sorbed in Li_2TiO_3 single crystal, J. Nucl. Mater. **442**, S437 (2013).

[19] K. Azuma, C. Dover, D. C. Grinter, R. Grau-Crespo, N. Almora-Barrios, G. Thornton, T. Oda, and S. Tanaka, J. Phys. Chem. C **117**, 5126 (2013).

[20] K. Azuma, T. Oda, and S. Tanaka, First-principles calculations for the surface termination of Li_2TiO_3(001) Surfaces, J. Nucl. Mater. **442**, S705 (2013).

[21] K. Kataoka, Y. Takahashi, N. Kijima, H. Nagai, J. Akimoto, Y. Idemoto, and K. Ohshima, Crystal growth and structure refinement of monoclinic Li_2TiO_3, Mater. Res. Bull. **44**, 168 (2009).

[22] N. V. Tarakina, R. B. Neder, T. A. Denisova, L. G. Maksimova, Y. V. Baklanova, A. P. Tyutyunnik, and V. G. Zubkov, Defect crystal structure of new $TiO(OH)_2$ hydroxide and related lithium salt Li_2TiO_3, Dalton Trans. **39**, 8168 (2010).

[23] H. A. Bumstead and R. G. V. Name, *Scientific Papers of Josiah Willard Gibbs*, Vol. I *Thermodynamics* (Longmans, Green, London, New York, 1906).

[24] K. Reuter and M. Scheffler, Composition, structure, and stability of RuO_2 (001) as a function of oxygen pressure, Phys. Rev. B **65**, 035406 (2001).

[25] P. Kratzer, E. Penev, and M. Scheffler, Understanding the growth mechanisms of GaAs and InGaAs thin films by employing first-principles calculations, Appl. Surf. Sci. **216**, 436 (2003).

[26] G.-X. Qian, R. M. Martin, and D. J. Chadi, First-principles study of the atomic reconstructions and energies of Ga- and As- stabilized GaAs(100) surfaces, Phys. Rev. B **38**, 7649 (1988).

[27] J. Padilla and D. Vanderbilt, *Ab initio* study of $BaTiO_3$ surfaces, Phys. Rev. B **56**, 1625 (1997).

[28] K. Rapcewicz, B. Chen, B. Yakobson, and J. Bernholc, Consistent methodology for calculating surface and interface energies, Phys. Rev. B **57**, 7281 (1998).

[29] M. W. Finnis, Accessing the excess: An atomistic approach to excesses at planar defects and dislocations in ordered compounds, Phys. Stat. Sol. A **166**, 397 (1999).

[30] A. Pojani, F. Finocchi, and C. Noguera, Polarity on the $SrTiO_3$ (111) and (110) surfaces, Surf. Sci. **442**, 179 (1999).

[31] X.-G. Wang, A. Chaka, and M. Scheffler, Effect of the environment on a-Al_2O_3 (0001) surface structures, Phys. Rev. Lett. **85**, 3225 (2000).

[32] E. Heifets, S. Piskunov, E. A. Kotomin, Y. F. Zhukovskii, and D. E. Ellis, Electronic structure and thermodynamic stability of double-layered $SrTiO_3$ (001) surfaces: *Ab initio* simulations, Phys. Rev. B **75**, 115417 (2007).

[33] R. Astala and M. J. Stott, First-principles study of hydroxyapatite surfaces and water absorption, Phys. Rev. B **78**, 075427 (2008).

[34] Y. A. Mastrikov, E. Heifets, E. A. Kotomin, and J. Maier, Atomic, electronic and thermodynamic properties of cubic and orthorhombic $LaMnO_3$ surfaces, Surf. Sci. **603**, 326 (2009).

[35] A. Dannenberg, M. E. Gruner, A. Hucht, and P. Entel, Surface energies of stoichiometric FePt and CoPt alloys and their implications for nanoparticle morphologies, Phys. Rev. B **80**, 245438 (2009).

[36] H. Seo and A. A. Demkov, First-principles study of polar $LaAlO_3$ (001) surface stabilization by point defects, Phys. Rev. B **84**, 045440 (2011).

[37] Q.-J. Liu, Z.-T. Liu, L.-P. Feng, H. Tian, and W. Zeng, Orthorhombic $SrHfO_3$ (001) surfaces: Surface structure and electronic properties with first-principles calculations, Comput. Theor. Chem. **989**, 59 (2012).

[38] A. Slepko and A. A. Demkov, First principles study of hydroxyapatite surface, J. Chem. Phys. **139**, 044714 (2013).

[39] H. Chen, H.-T. Yu, and Y, Xie, First-principles investigation of stability diagram and electronic properties of $SrHfO_3$ (110) Polar terminations, Mater. Chem. Phys. **174**, 195 (2016).

[40] H. Ren, W.-C. Hu, D.-J. Li, X.-Q. Zeng, X. Yang, X.-S. Zeng, X.-J. Yang, B. Huang, and Y. Liu, Atomic relaxation, stability and electronic properties of Mg_2Sn (100) surfaces from *ab-initio* calculations, J. Mag. Alloy. **4**, 62 (2016).

[41] J. W. Kaminski, P. Kratzer, and C. Ratsch, Towards a standardized setup for surface energy calculations, Phys. Rev. B **95**, 085408 (2017).

[42] Y. Zhang, J. Zhang, and J. Zhu, Phys. Rev. Mater. **2**, 073401 (2018).

[43] G. Hautier, S. P. Ong, A. Jain, C. J. Moore, and G. Ceder, Accuracy of density functional theory in predicting formation energies of ternary oxides from binary oxides and its implication on phase stability, Phys. Rev. B **85**, 155208 (2012).

[44] G. Kresse and J. Hafner, *Ab initio* molecular dynamics for liquid metals, Phys. Rev. B **47**, 558 (1993).

[45] G. Kresse and J. Furthmüller, Efficient iterative schemes for *ab initio* total-energy calculations using a plane-wave basis set, Phys. Rev. B **54**, 11169 (1996).

[46] G. Kresse and D. Joubert, From ultrasoft pseudopotentials to the projector augmented-wave method, Phys. Rev. B **59**, 1758 (1999).

[47] J. P. Perdew, K. Burke, and M. Ernzerhof, Generalized gradient approximation made simple, Phys. Rev. Lett. **77**, 3865 (1996).

[48] S. T. Murphy, P. Zeller, A. Chartier, and L. V. Brutzel, Atomistic Simulation of the Structural, Thermodynamic, and Elastic Properties of Li_2TiO_3, J. Phys. Chem. C **115**, 21874 (2011).

[49] S. T. Murphy, Tritium solubility in Li_2TiO_3 from first-principles simulations, J. Phys. Chem. C **118**, 29525 (2014).

[50] M. M. Islam and T. Bredow, Lithium diffusion pathways in β-Li_2TiO_3: A theoretical study, J. Phys. Chem. C **120**, 7061 (2016).

[51] Y. Shi, J. Qi, Y. Han, and T. Lu, Anisotropic diffusion of a charged tritium interstitial in Li_2TiO_3 from first-principles calculations, Phys. Rev. Appl. **10**, 024021 (2018).

[52] K. Li, W. Yang, W.-H. Wang, and Y.-T. Li, First principles study of tritium diffusion in Li_2TiO_3 crystal with lithium vacancy, Materials **11**, 2383 (2018).

[53] Y. Hosogi, H. Kato, and A. Kudo, Visible light response of $AgLi_{1/3}M_{2/3}O_2$ (M = Ti and Sn) synthesized from layered Li_2MO_3 using molten $AgNO_3$, J. Mater. Chem. **18**, 647 (2008).

[54] E. J. Covington and D. J. Montgomery, Lattice constants of separated lithium isotopes, J. Chem. Phys. **27**, 1030 (1957).

[55] R. M. Wood, The lattice constants of high purity alpha titanium, Proc. Phys. Soc. **80**, 783 (1962).

[56] W. J. Orville-Thomas, A bond-order/bond-length relation for oxygen-oxygen bonds, J. Mol. Spectrosc. **3**, 588 (1958).

[57] S. Hull, T. W. D. Farley, W. Hayes, and M. T. Hutchings, The elastic properties of lithium oxide and their variation with temperature, J. Nucl. Mater. **160**, 125 (1988).

[58] J. K. Burdett, T. Hughbanks, G. J. Miller, J. W. Richardson, Jr., and J. V. Smith, Structural-electronic relationships in inorganic solids: Powder neutron diffraction studies of the rutile and anatase polymorphs of titanium dioxide at 15 and 295 K, J. Am. Chem. Soc. **109**, 3639 (1987).

[59] K. Oura, M. Katayama, A. V. Zotov, V. G. Lifshits, and A. A. Saranin, *Surface Science* (Springer, Berlin, Heidelberg, 2003).

[60] A private communication with Prof. Geoff Thornton indicates that the period of the ordered hexagonal-like pattern in the STM images is about 0.5 nm instead of about 0.4 nm in Ref. [19].

[61] J. Tersoff and D. R. Hamann, Theory of the scanning tunneling microscope, Phys. Rev. B **31**, 805 (1985).